City Research Online

City, University of London Institutional Repository

Citation: Kyriazis, N., Koukouvinis, P. & Gavaises, M. (2018). Modelling cavitation during drop impact on solid surfaces. Advances in Colloid and Interface Science, 260, pp. 46-64. doi: 10.1016/j.cis.2018.08.004

This is the accepted version of the paper.

This version of the publication may differ from the final published version.

Permanent repository link: https://openaccess.city.ac.uk/id/eprint/20484/

Link to published version: https://doi.org/10.1016/j.cis.2018.08.004

Copyright: City Research Online aims to make research outputs of City, University of London available to a wider audience. Copyright and Moral Rights remain with the author(s) and/or copyright holders. URLs from City Research Online may be freely distributed and linked to.

Reuse: Copies of full items can be used for personal research or study, educational, or not-for-profit purposes without prior permission or charge. Provided that the authors, title and full bibliographic details are credited, a hyperlink and/or URL is given for the original metadata page and the content is not changed in any way.

City Research Online: http://openaccess.city.ac.uk/ publications@city.ac.uk

Modelling cavitation during drop impact on solid surfaces

Nikolaos Kyriazis[a,*], Phoevos Koukouvinis[a], Manolis Gavaises[a]

[a]*School of Mathematics, Computer Science & Engineering, Department of Mechanical Engineering & Aeronautics, City University London, Northampton Square EC1V 0HB, United Kingdom.*

Abstract

The impact of liquid droplets on solid surfaces at conditions inducing cavitation inside their volume has rarely been addressed in the literature. A review is conducted on relevant studies, aiming to highlight the differences from non-cavitating impact cases. Focus is placed on the numerical models suitable for the simulation of droplet impact at such conditions. Further insight is given from the development of a purpose-built compressible two-phase flow solver that incorporates a phase-change model suitable for cavitation formation and collapse; thermodynamic closure is based on a barotropic Equation of State (EoS) representing the density and speed of sound of the co-existing liquid, gas and vapour phases as well as liquid-vapour mixture. To overcome the known problem of spurious oscillations occurring at the phase boundaries due to the rapid change in the acoustic impedance, a new hybrid numerical flux discretization scheme is proposed, based on approximate Riemann solvers; this is found to offer numerical stability and has allowed for simulations of cavitation formation during drop impact to be presented for the first time. Following a thorough justification of the validity of the model assumptions adopted for the cases of interest, numerical simulations are firstly compared against the Riemann problem, for which the exact solution has been derived for two materials with the same velocity

*Corresponding author

Email addresses: Nikolaos.Kyriazis@city.ac.uk (Nikolaos Kyriazis), Foivos.Koukouvinis.1@city.ac.uk (Phoevos Koukouvinis), M.Gavaises@city.ac.uk (Manolis Gavaises)

and pressure fields. The model is validated against the single experimental data set available in the literature for a 2-D planar drop impact case. The results are found in good agreement against these data that depict the evolution of both the shock wave generated upon impact and the rarefaction waves, which are also captured reasonably well. Moreover, the location of cavitation formation inside the drop and the areas of possible erosion sites that may develop on the solid surface, are also well captured by the model. Following model validation, numerical experiments have examined the effect of impact conditions on the process, utilising both planar and 2-D axisymmetric simulations. It is found that the absence of air between the drop and the wall at the initial configuration can generate cavitation regimes closer to the wall surface, which significantly increase the pressures induced on the solid wall surface, even for much lower impact velocities. A summary highlighting the open questions still remaining on the subject is given at the end.

Keywords: Cavitation, drop impact, approximate Riemann solvers, OpenFOAM

---

1. Introduction

Droplets impacting onto solid or liquid surfaces are of significant importance in many engineering applications, oceanography, food science and even forensics; see selectively [1, 2, 3, 4, 5, 6] among many others. For isothermal conditions, the Weber We, Reynolds Re, Ohnesorge Oh and Froude Fr numbers are frequently utilised to characterise the droplet impact outcome; these are defined as $\mathrm{We} = \frac{\rho_l u_{imp}^2 D}{\sigma}$, $\mathrm{Re} = \frac{\rho_l u_{imp} D}{\mu_l}$, $\mathrm{Oh} = \frac{\sqrt{\mathrm{We}}}{\mathrm{Re}}$ and $\mathrm{Fr} = \frac{u_{imp}}{\sqrt{gD}}$, respectively. In these relations, u_{imp} is the impact velocity normal to the wall surface, D is the droplet diameter, μ_l and ρ_l are the dynamic viscosity and density of the liquid droplet respectively, σ is the surface tension and g is the gravitational acceleration. A number of post-impact outcomes are known for the normal/inclined impact of spherical droplets onto flat and smooth surfaces [7, 8]. In the vast majority among the cases of practical interest, the flow conditions and the evo-

lution of the droplet shape upon impact can be described assuming that the liquid and the surrounding media behave as incompressible media. Still, out of the very broad literature on the subject, or interest to the present paper are the cases of impact at velocities of the order of $200\,m/s$ ($M \approx 0.6$ for air at room temperature and atmospheric pressure) which are high enough for compressibility effects to become important. Moreover, at such conditions pressure waves developing within the liquid during impact may induce cavitation formation within the droplet volume. Cavitation as a phenomenon involves the formation of vaporous/gaseous cavities in the bulk of liquid, due to localized static pressure drop. This can happen due to strong accelerations, high velocities or pressure waves. In the first case, cavitation is termed as 'hydrodynamic' and may occur in any device operating with liquids, e.g. propellers, turbines, pumps, valves etc. In the second case, cavitation is termed as 'acoustic', since it is induced by the presence or interaction of acoustic waves. Phase-change during cavitation is inertial driven [3] as opposed to phase-change processes driven by the temperature difference between the liquid, air and the solid surface. Moreover, for the high impact velocity conditions leading to cavitation formation, the impact outcome is expected to be in the splashing regime, where a corona is initially formed and gradually disintegrates into a number of droplet fragments. Such impact velocities can be realised, for example, in steam turbines and aircraft components. The steam in the turbine engine operating at low pressure conditions is prone to condensation and thus, water droplets are formed. These droplets travel with the flow and can impact the turbine blades with high speeds [2, 9]. The problem is further complicated by the subsequent cavitation formation and collapse induced by the pressure waves developing within the droplet's volume. At such conditions, surface erosion and damage may occur, not only because of the impact pressure, but also due to the pressure increase occurring during the collapse of the cavitation bubbles. The early experimental work of Field et al. [10] documented that the edge pressures depend on the impact velocity and the angle between the liquid and the solid surfaces (see also [11]). More recently, Field et al. [12] presented high-speed images of impacted

liquids using several different techniques. By adding gelatine in the water, they produced 2-D planar 'droplets' between two transparent plates while impact was achieved by a projected third plate. The shock waves produced and the resulting vapour formation due to cavitation within the bulk of liquid has been observed qualitatively. So far, no other studies are known in this field. The present paper aims to contribute to this area by conducting initially a literature review on the subject, followed by numerical simulations from a purpose-built computational model. The literature review starts with a summary of relevant numerical works for droplet impact of incompressible liquids. Then a short review on phase-change models and numerical methodologies for cavitation, relevant to the current study is included, followed by a review of the studies that have addressed the role of compressibility during droplet impact. As already mentioned, in the absence of computational studies in the literature for droplet impact in the presence of cavitation formation and subsequent collapse, the paper presents results from a newly developed computational fluid dynamics flow solver suitable for such conditions. Following validation against the experiments of [12], parametric studies aim to provide further inside on the problem physics.

2. Literature Review

2.1. Summary of methodologies applied to droplet impact assuming incompressible liquids

Both experiments and complex numerical simulations based on the solution of the Navier-Stokes equations have been utilised to characterise the impact process of liquid droplet onto solid or liquid surfaces. Within the context of incompressibility and at conditions that surface tension (i.e. sufficiently small We numbers) dominates the temporal development of the phenomenon, Lagrangian (interface tracking) and Eulerian (interface capturing) approaches, or even a combination of the two have been utilised to simulate the process. For example, Harlow and Shannon [13] where the first to utilise the Lagrangian approach using a marker-and-cell (MAC) finite difference algorithm ignoring surface tension

and viscosity, while the volume of fluid (VOF) model was introduced by Hirt and Nichols [14]; later Youngs [15] proposed a 3-D volume tracking algorithm (see also [16]). Aniszewski et al. [17] made a comparative study among different VOF methodologies. Numerous follow-up studies have addressed the problem under various impact conditions [18, 19, 20], different fluids [21], elevated wall temperatures [22], impact on non-flat [23, 24] or complex [25, 6] surfaces and impact of stream of droplets [26, 27]. Apart from the VOF method, the Piecewise linear Interface Calculation (PLIC) approach [28, 29], the Weighted Linear Interface Calculation (WLIC) method, which was introduced by Yokoi [30] and independently by Marek et al. [31] and the Tangent of Hyperbola for Interface Capturing (THINC) interface reconstruction scheme, which was described by [32]; the more recent works of [33, 34] are an extension of THINC scheme. Fukai et al. [7] developed a finite element model (FEM) for the incompressible flow equations but the hyperbolic character of the equations was obtained by the artificial compressibility method. Although the VOF method was originally developed and has been mainly used for incompressible flows, it has been also extended to compressible fluids, see for example [33, 35, 36, 37, 38, 39]. Nowadays, VOF methods with arbitrary unstructured meshes have become popular and have been implemented in the open source CFD toolbox OpenFOAM [40, 41]. Along these lines, Gerris, an open source incompressible VOF solver with adaptive mesh refinement capabilities, originally developed by Popinet [42], has been used for two-phase flows where surface tension is prevalent but without modelling phase-change phenomena (see also [43]). Overall, such methods are in principle applicable to cases with cavitation developing during the droplet impact; however, as it is demonstrated later, accurate modelling of the liquid-gas interface becomes important at time scales much longer than the cavitation formation and collapse, and thus these methods are less important or can be even not accounted for such problems.

2.2. Models for cavitation and interaction with surfaces

As the physics and relevant models for cavitation are the primary focus of the present work, an extended summary of models is provided. The review considers models applicable both to microscales (single bubble collapses) or cavitation clouds comprising a large population of bubbles and thus more suitable for problems of engineering interest. The thermodynamic closure of such models is also briefly addressed.

2.2.1. Models suitable for single-bubbles (microscales)

From a historical perspective, interaction of cavitation bubble collapse with a nearby solid surface has been studied since 1970 [44] (see also the experimental works of Launterborn et al. [45, 46, 47]). Along similar lines are the investigations of [48, 49] on bubble deformation and collapse near a wall, employing the Boundary Element Method (BEM). This method is still being used for high fidelity bubble simulations [50] and interactions with deformable bodies [51, 52]. Despite its relative simplicity and accuracy, BEM is susceptible to instabilities and it is difficult to handle topological changes of the bubble interface [53], which require regularization and smoothing. Moreover, the potential solver, at the core of BEM, lacks small scale dissipative mechanisms leading to singularities [54]. Extensions of BEM involve Euler/Navier-Stokes flow solvers, which may include compressibility effects as well and sharp interface/ interface capturing/tracking techniques [55]. More recent work employs multiphase flow techniques for handling of the gas/liquid interface [56, 57] using a Homogeneous Equilibrium Model. Apart from single fluid approaches, various interface tracking methodologies have been employed for the prediction of pressure due to bubble collapse. A notable example of high-end simulations of bubble cloud collapse is [58]; the authors performed simulation of a resolved bubble cloud, consisting of $15,000$ bubbles in the vicinity of a wall, using a supercomputer. Representative studies using the Volume Of Fluid (VOF) approach to predict bubble collapses and jetting phenomena include [59, 60, 61]. Instead of VOF, other authors [62, 63] used the Level Set (LS) technique for analyzing the effect

of different bubbles at different distances from nearby walls. Both techniques have their advantages and disadvantages; VOF ensures conservation, whereas LS offers high accuracy calculation of the interface curvature and surface tension. An alternative to interface tracking methodologies is the front tracking method [54], such as the one used in [64] for the simulation of gas bubbles collapsing in finite/infinite liquid domains. This method differs from VOF or LS, in the sense that the interface is explicitly tracked by a set of Lagrangian marker points that define the interface topology, enabling high fidelity simulations and predictions to be made, without smearing of the interface. Assessing current methodologies, the treatment of the vapour/gas and liquid mixture, both Homogeneous Equilibrium [57] or non-equilibrium interface tracking immiscible fluid methodologies are applicable. While both methodologies have been successfully employed for studying the pressure field generated on the wall due to the collapse of nearby bubbles for various configurations, the methodology of interface capturing is definitely less restricting, allowing one to simulate gaseous/vaporous mixtures within the bubble, while also prescribing finite rate of mass transfer and giving the opportunity of imposing surface tension, which is important in the case of bubble nucleation. The front tracking method has the advantage of being capable of incorporating the capabilities of the interface tracking and the two fluid approach, without interface diffusion; however, it is somewhat problematic in complicated interface topologies [65]. With regards to simultaneous simulations of pressures resulting from the collapse of cavitating bubbles and material response to induced load, very few studies have been published [66, 67, 68].

2.2.2. Cavitation models suitable for engineering scales

Cavitation models applied to length/time scales of practical or engineering interest, can be classified into three categories. The first approach invokes the thermodynamic equilibrium assumption, leading to an effective mixture equation of state that returns the vapour volume fraction directly from the cell-averaged fluid state [56]. As this mixture model constitutes a natural sub-grid scale model for the thermodynamic fluid state, recovering the limit of individ-

ual bubbles for sufficient resolution, it can be employed within a physically motivated implicit LES approach [69]. Whereas all practical applications in engineering relevant cases at high ambient pressures indicate that the equilibrium model gives the correct prediction in terms of cavitation and wave dynamics, detailed investigations of incipient cavitation or wall-bubble interactions may depend on other processes, for example, gas content, wall crevices and local heating effects. For such phenomena at single bubbles, interfacial effects are potentially important and can be treated by sharp-interface methods [70, 56]. The second approach is based on the introduction of a rate equation for the generation of vapour that employs explicit source/sink terms. Both Eulerian-Eulerian and Eulerian-Lagrangian formulations can be used to track the vapour production and its interaction with the liquid. For example, Eulerian-Eulerian models use a bubble-cloud model applied to Reynolds-averaged turbulence modelling [71, 72] and LES. In the model of [73] instead of treating cavitation as a single mixture, the two-fluid method was employed; two sets of conservation equations are solved, one for the liquid and one for the vapour phase. With this approach the two phases can have different velocities. Another variant of the bubble model is the approach of [74, 75] in which the classical interface capturing Volume of Fluid (VOF) method was utilised for simulating the scalar volume fraction of a bubble cloud. Similar models are currently available in commercial CFD models [76, 77, 78]. Typically, these models utilize the asymptotic form of the Rayleigh-Plesset equation of bubble dynamics. They all require information on the bubble number density and population present in the liquid prior to the onset of cavitation, while, depending on their complexity and sophistication, they may include or ignore mass transfer between the liquid and the vapour phases and may consider or not gas content in the liquid. It is clear that at their current state such models require case-by-case tuning of the involved parameters in order to predict realistic cavitation images.

The Eulerian-Lagrangian formulation also aims to provide a coupling between the interaction between the liquid (Eulerian) and vapour (Lagrangian) states. One of the most important models in this category is the Lagrangian

cavitation model of [79, 80] that uses the Rayleigh-Plesset equation of bubble dynamics for estimating the cavitation volume fraction. More recent advances (selectively [81, 82, 83]) have proposed models that account for collective compressibility and shock wave interaction effects in polydispersed cavitating flows. Some models do exist for predicting the collapse process of individual vapour/air bubbles or bubble clouds within the bulk of the liquid or even near a wall surface (selectively [84, 85, 86, 87]) but most of them have not been applied to flows of industrial interest while effects such as chemical composition change, heat transfer and liquid heating are ignored. It is also worth mentioning that effects of dissolved gas, multi-component fluids (such as fuels) and pre-existing nucleation sites in the fluid have not been investigated so far.

The third approach for describing cavitation effects is by employing Probability Density Functions (PDF) and related transport models. In [88] a PDF transport model is used for the vapour fraction, based on the Boltzmann transport equation, in order to model the highly dynamic and stochastic interaction of the turbulent flow field with the cavitation structures. An additional novelty of [88] is the fact that the solution of the PDF is done entirely in an Eulerian framework, avoiding the expensive cost and the inaccuracies induced by coupling an Eulerian and Lagrangian solver. The authors have shown that by coupling the PDF method with a compressible LES framework, they obtained good results for a variety of Venturi-like tubes and shapes. The applicability of such models to engineering-scale problems has not been tested yet. Finally, apart from the aforementioned models, which are based on the finite volume framework, there have been efforts for describing cavitation using alternative frameworks. Examples of such works may include (a) simulation of cavities due to the entry of high speed objects, using the mesh-less Smoothed Particle Hydrodynamics (SPH) [89] and the Finite Element method (FEM) [90], (b) simulation of cavities at the wake of submerged bodies in liquid [91], using Distributed Particle Methods and focusing on the SPH method in particular, (c) simulations of forward step geometries, resembling the orifice of injectors, using Lattice Boltzmann methodologies [92]. These examples are, of course,

non-exhaustive. There are many different approaches, most of them at an infancy stage, for attacking the phenomenon of cavitation, each having specific advantages and disadvantages on specific flow types. On the other hand, the Finite Volume framework is mature enough and offers better handling of the underlying flow phenomena with less uncertainties over the physics for general flow types.

2.2.3. Thermodynamic closure

A common issue that is found in bubble dynamics simulations in the recent literature is the EoS of the materials involved and, more generally, material properties and their variation in respect to pressure and temperature. It is well known that gas/vapour bubbles may be at sub-atmospheric conditions when at maximum size, but during the last stages of the collapse pressures may reach the order of GPa and temperatures the magnitude of several thousand Kelvin. In the literature, however, it is commonly assumed that liquids behave according to the stiffened gas EoS and the gas/vapour as an ideal gas [58, 93, 94] despite the strong evidence that the stiffened gas EoS may not be adequate, since it cannot replicate at the same time both the correct density and the speed of sound of the liquid [95]. For this reason, many researchers have recently turned towards more accurate relationships for describing the materials involved [57] and [96] developed by the authors. Such accurate EoS have been formulated by NASA [97, 98] or in other investigations [99].

The value of the calculated pressures on the wall can be indicative of the loading expected. However, these are subject to grid resolution, as mentioned earlier. Moreover, erosion is observed after long operation time, which is something that is not addressed here.

2.3. Droplet impact and compressibility effects

The aforementioned studies regarding cavitation have never been applied so far to cases of droplet impact. There are some studies addressing compressibility effects but they have been considered only in a small part of the relevant liter-

ature. The analytic solutions of Heymann [100] and Lesser [101] were the first to consider compressibility. Heymann [100] performed a quasi-steady state 2-D analysis of the dynamics of impact between a compressible liquid droplet and a rigid surface. However, this analysis is only valid for the initial stages of the impact, during which the shock is attached to the solid surface, so the jetting in the contact edge could not be predicted. Later on, Lesser [101] expanded this work and took into account the elasticity of the surface while he also gave an analytic solution of the 3-D droplet impact problem (see also [6]). Numerical simulations have been also employed. For example, a front tracking solution procedure was proposed by Haller et al. [102] for high-speed impact of small size droplets. A rectangular finite difference Eulerian grid and a moving lower dimension Lagrangian one to track the location of the wave fronts have been utilized (see also [103]). In another compressible approach, Sanada et al. [104] used the multicomponent Euler equations to model high-speed droplet impact. They developed a third-order WENO scheme with an HLLC Riemann solver and the time advancement was achieved by a third-order TVD Runge-Kutta. More recently, Niu and Wang [105] developed a compressible two-fluid model for the Euler equations and they proposed an approximated linearized Riemann solver for the liquid-gas interface. Surface tension was neglected due to high We number, as well as in the above high-speed droplet impacts. Furthermore, they showed that higher impact speed results in higher impact pressure and possible damage in the solid surface. Algorithms able to handle liquid-gas interface have been also developed by Lacaze et al. [106], Örley et al. [107] and Gnanaskandan and Mahesh [108] but droplet impacts have not been simulated so far. More recently, Shukla et al. [35] solved the multi-component compressible flow equations with an interface compression technique aiming to capture the thickness of the interface within a few cells. Summarising, it can be said that although vast number of studies are available for compressible flows, these have not been applied so far to cases of droplet impact at conditions inducing cavitation within its volume.

2.4. The present contribution

With the exception of the observations of Field et al. [12], to the author's best knowledge, there is no other experiment and no numerical study published in which the formation and development and cavitation within the bulk of the impacting droplet is considered; the only relevant numerical study is the work of Niu et al. [105], where cavitation zones have been identified but without actually simulating the phase-change process. The aforementioned experimental data of Field et al. [12] have not been so far simulated by any of the studies available in the open literature.

This problem is addressed here for the first time using a newly developed numerical algorithm implemented in OpenFOAM. For modelling cavitation, the thermodynamic closure is achieved by a barotropic approach for the three phases [107]. In order to keep the conservative form of the solved equations, the gas phase is modelled by a VOF-like method. Moreover, a hybrid numerical flux, which is free of numerical dispersion in the phase boundaries and suitable for a wide range of Mach number flows, is also proposed. The numerical model is utilised to demonstrate and quantify the effect of pressure-driven phase change taking within the drop's volume during the initial stages of impact. The pressures induced on the solid wall during the collapse of cavitation are computed as function of the impact conditions and are compared to those resulting from the impact itself. Moreover, the influence they have of the temporal development of the splashing liquid during the initial stages of impact are explained.

The paper is organized as follows. In the following section, the numerical method is described, including the EoS for the three phases and the time/space discretization employed. Then the results are presented and discussed; verification and validation of the numerical method is performed against the the exact Riemann problem and the 2-D drop impact experiment [12], respectively. Then a parametric study utilising 2-D axisymmetric drop impacts is performed for different impact velocities; the most important conclusions are summarised at the end. Finally, in Appendix A, the methodology for deriving the exact solution to the Riemann problem for the multi-material Euler equations is discussed; this

methodology was used to obtain the exact solution for the benchmark Riemann problem. In Appendix B, the temperature difference in an isentropic compression process is calculated, justifying that way the choice of the barotropic EoS.

3. Numerical Method

In this section, the developed numerical methodology (2phaseFoam), able to predict liquid, vapour and gaseous phases co-existence under equilibrium conditions has been developed in OpenFOAM [109]; this has been based on the single-phase solver rhoCentralFoam. Initially, the main assumptions adopted for the application of the model to drop impact cases inducing cavitation are justified, followed by the mathematical description of the model itself.

3.1. Model assumptions

For the cases of drop impact investigated here, the flow can be considered inertia driven since the Reynolds number Re is 10^6; typically this is calculated for impact velocity $110\,m/s$, $D = 10\,mm$, $\rho_l = 998.207\,kg/m^3$ and thus, the viscous effects can be neglected. Moreover, interest is focused primarily during the initial stages of impact when cavitation formation and its subsequent collapse take place; these occur during the early stages of splashing which is also inertia driven, so the solution of the Euler equations instead of the full Navier-Stokes are rendered suitable for capturing the relevant physics. Furthermore, the minimum Weber number We in the present drop impact simulations is calculated to be around 10^5 and thus, surface tension is negligible; the minimum Froude number Fr is 88 and therefore the gravitational forces are insignificant compared to inertia. Due to the high impact velocities which result in high We and therefore neglecting the surface tension, contact angle boundary conditions are not explicitly defined. Zero gradient boundary condition in the transport equation for the gas mass fraction is used at the wall instead (equivalent to a contact angle of 180°). Surface wettability plays an important role only when a low velocity field is noticed in the lamella and therefore adhesion forces become

significant [25]. However, in the present study the lamella velocity is approximately 10 times higher than the $u_{imp} = 110\, m/s$ and therefore such effects are ignored.

In the HEM approach which is followed in the present work, infinite nucleation points and infinite mass transfer rate are assumed, so thermodynamic equilibrium is achieved instantaneously. In order to add nucleation sites in the Eulerian framework, a mass transfer model is necessary, such as the Singhal model [75], the Zwart-Gerber-Belamri Model [110] or similar. However, such models are empirical and case dependent and thus, tuning is necessary. Alternatively, an Eulerian approach for the liquid and a Lagrangian method for the discrete bubbles based on the modified Rayleigh-Plesset equation has been employed in [111, 112, 113]. Apart from having a restricted validity for spherical bubbles, which is a strong assumption, such models significantly increase the computational cost. All things considered, the Eulerian diffuse interface approach, which is not possible to capture discrete nucleation sites has been utilized here as a compromise between model complexity and numerical efficiency and due to lack of information for the composition and the character of the nuclei [114]. This methodology has been demonstrated to accurately predict the Rayleigh collapse of vaporous structures (see [107, 115, 116]). Given the original configuration and the final simulation time, which corresponds to the early stages of drop splashing, sharp interface algorithms have not been used in the present study. The drop is initially placed next to the wall impinging with velocity u_{imp} into stagnant air and as a consequence, there is no drop motion in the air before the impact. The latter would necessitate sharp interface schemes in order to avoid having a diffusive interface while the drop is travelling in the air. In addition, at later stages of splashing, which are not simulated in the present study, sharp interface algorithms are necessary in order to provide a smear-free interface. Finally, temperature effects are not taken into account in the present study, since they are negligible. The interested reader is addressed to Appendix B, where this assumption is justified.

3.2. Governing equations

The three dimensional compressible Euler equations in conservative form are considered:

$$\frac{\partial \mathbf{U}}{\partial t} + \frac{\partial \mathbf{F}_k(\mathbf{U})}{\partial x_k} = 0, \quad in \quad \Omega, \tag{1}$$

where $k = 1, 2, 3$ denotes the x, y, z directions. The following initial and boundary conditions are used for the PDE system:

$$\mathbf{U}(\mathbf{x}, \mathbf{0}) = \mathbf{U_0}(\mathbf{x}), \quad \textbf{in} \quad \mathbf{\Omega}, \tag{2}$$

$$\mathbf{U} = \mathbf{U_D}, \quad \textbf{on} \quad \partial\mathbf{\Omega_D}, \tag{3}$$

$$\frac{\partial \mathbf{U}}{\partial \mathbf{n}} = \mathbf{U_N}, \quad \textbf{on} \quad \partial\mathbf{\Omega_N}, \tag{4}$$

where

$$\mathbf{U} = \begin{bmatrix} \rho & \rho Y_g & \rho u_1 & \rho u_2 & \rho u_3 \end{bmatrix}^{\mathbf{T}}$$

is the conservative solution vector, ρ is the mixture density, ρY_g is the gas mass fraction and $\rho\mathbf{u}$ is the mixture momentum. Here the absence of the energy equation is due to the barotropic approach (see section 3.3), whereas a transport equation for modelling the non-condensable gas phase is used. The flux tensor $\bar{\bar{\mathbf{F}}}$ is the convective term and can be analysed into x, y and z components: $\bar{\bar{\mathbf{F}}} = \begin{bmatrix} \mathbf{F_1} & \mathbf{F_2} & \mathbf{F_3} \end{bmatrix}$, where:

$$\mathbf{F_1} = \begin{bmatrix} \rho u_1 \\ \rho Y_g u_1 \\ \rho u_1^2 + p \\ \rho u_1 u_2 \\ \rho u_1 u_3 \end{bmatrix}, \quad \mathbf{F_2} = \begin{bmatrix} \rho u_2 \\ \rho Y_g u_2 \\ \rho u_2 u_1 \\ \rho u_2^2 + p \\ \rho u_2 u_3 \end{bmatrix} \quad \mathbf{F_3} = \begin{bmatrix} \rho u_3 \\ \rho Y_g u_3 \\ \rho u_3 u_1 \\ \rho u_3 u_2 \\ \rho u_3^2 + p \end{bmatrix} \tag{5}$$

3.3. Thermodynamic Model

A homogeneous-mixture approach is used for describing the liquid, liquid-vapour regime (referred as mixture from now on) and gas phases, which means that the three phases are in mechanical and thermal equilibrium. The mixture density ρ is:

$$\rho = \beta_{lm}[\ (1-\alpha_v)\rho_l + \alpha_v\rho_v] + \beta_g\rho_g, \tag{6}$$

In the above relation, the subscripts l, m, g represent the liquid, mixture and gas regimes respectively, whereas lm refers to the liquid-vapour mixture which is governed by a single EoS and it is treated as a single fluid. The volume fraction is denoted by β and α is the local volume fraction. The density of the component $i = l, m, g$ can be found from:

$$\rho_i = \frac{m_i}{V_i} = \frac{Y_i m}{\beta_i V} = \frac{Y_i}{\beta_i}\rho, \tag{7}$$

where the volume fraction β of the i component is:

$$\beta_i = \frac{V_i}{V}, \quad \sum_i \beta_i = 1, \tag{8}$$

the mass fraction Y_i of the i component is:

$$Y_i = \frac{m_i}{m}, \quad \sum_i Y_i = 1, \tag{9}$$

and the local volume fraction can be calculated from the formula:

$$\alpha_v = \begin{cases} 0, & \rho \geq \rho_{l,sat} \\ \beta_{lm}\frac{\rho_{l,sat}-\rho_{lm}}{\rho_{l,sat}-\rho_{v,sat}}, & \rho < \rho_{l,sat} \end{cases} \tag{10}$$

The single fluid model for the liquid and mixture is extended by a transport equation for the non-condensable gas. A linear barotropic model has been utilized for the pure liquid and mixture (lm). The density ρ_{lm} of the latter is:

$$\rho_{lm} = \rho_{l,sat} + \frac{1}{c^2}(p - p_{sat}), \quad c = \begin{cases} c_l, & p \geq p_{sat} \\ c_m, & p < p_{sat} \end{cases} \tag{11}$$

where $\rho_{l,sat}$ is the density of the liquid at saturation condition and c is the speed of sound of the liquid or the mixture, depending on the saturation pressure p_{sat}. The gas phase, has been modelled by an isothermal ideal gas EoS and thus, the gas density is given by:

$$\rho_g = \frac{p}{R_g T_{ref}}, \tag{12}$$

where the reference temperature is $T_{ref} = 293.15\,K$ and the specific gas constant is $R_g = 287.06\,J/(kg\,K)$. The barotropic approach is followed since the temperature difference in the following simulations is negligible (the interested reader is referred to Appendix B, where the temperature difference in an isentropic compression process is calculated).

Differentiating isentropically Eq. (11) with respect to density, constant speed of sound for the liquid and mixture is found for water: $c_l = 1482.35\,m/s$ and $c_m = 1\,m/s$, following Brennen [114] and Örley et al. [107]. For the ideal gas, the speed of sound is calculated from:

$$c_g = \sqrt{R_g T_{ref}}, \tag{13}$$

where the specific heat ratio $\gamma = \frac{C_p}{C_v}$ is unity (isothermal approach). In the three phase mixture, the speed of sound between lm and g phases is determined by the Wallis speed of sound [114, 117]:

$$\frac{1}{\rho c^2} = \frac{1-\beta_g}{\rho_{lm} c_{lm}^2} + \frac{\beta_g}{\rho_g c_g^2}, \tag{14}$$

In order to calculate the pressure of the mixture, a closed form equation of state describing the co-existence of three phases is employed from Eq. (6):

$$\rho = \beta_{lm}\Big[\rho_{l,sat} + \frac{1}{c^2}(p - p_{sat})\Big] + \beta_g \frac{p}{R_g T_{ref}}, \tag{15}$$

replacing the volume fraction β_g from Eq. (7) and eliminating β_{lm} by using Eq. (9) and Eq. (12), a quadratic equation for the pressure is derived:

$$Ap^2 + Bp + C = 0, \tag{16}$$

where

$$A = \frac{1}{c^2}, \tag{17}$$

$$B = \rho(Y_g - 1) + \rho_{l,sat} - \frac{p}{c^2} - \frac{Y_g \rho R_g T_{ref}}{c^2}, \tag{18}$$

$$C = Y_g \rho R_g T_{ref} \left(\frac{p_{sat}}{c^2} - \rho_{l,sat} \right). \tag{19}$$

In the case of two real solutions $p_1, p_2 \in \mathbb{R}$, the largest root of Eq. (16) is kept. The speed of sound in Eq. (17), (18) and (19) is set to either c_l or c_m, depending on the pressure at the previous time step for identifying the liquid or mixture regions. Therefore, Eq. (16) is solved iteratively, in case the computed pressure does not fulfil the original assumption. In practice, the algorithm is repeated for no more than three iterations.

3.4. Discretization

Due to the large variation in the speed of sound, the Mach number in three phase flows can range from 10^{-2} up to 10^2 or even higher [118]. As it can be seen in the previous sub-section from Eq. (13) and (11), the speed of sound can vary from $1\,m/s$ in the mixture regime, up to $1482.35\,m/s$ in the liquid region, whereas in the gaseous phase the speed of sound is $290\,m/s$. This is an obstacle in density-based solvers, since they are prone to slow convergence and dispersion in low Mach number flows [119, 120, 121]. In order to handle the low Mach number problem, a hybrid flux, suitable for multiphase flows, is proposed here for first time.

The aforementioned flux is based on the Primitive Variable Riemann Solver (PVRS) [122] and the Mach consistent numerical flux of Schmidt et al. [123]. That way, an efficient and robust solver is developed, by utilizing an approximated Riemann solver, instead of the exact one. At the same time, the numerical

scheme is suitable for subsonic up to supersonic flow conditions. The numerical inviscid flux in the k direction at the $i+1/2$ interface takes the following form:

$$\mathbf{F}_k^{i+1/2} = \rho^{L/R} u_k^\star \begin{bmatrix} 1 \\ Y_g^{L/R} \\ u_1^{L/R} \\ u_2^{L/R} \\ u_3^{L/R} \end{bmatrix} + p^\star \begin{bmatrix} 0 \\ 0 \\ \delta_{1k} \\ \delta_{2k} \\ \delta_{3k} \end{bmatrix}, \tag{20}$$

where the interface velocity $u_k^\star$ is approximated by:

$$u_k^\star = \frac{1}{C^L + C^R}[\, C^L u_k^L + C^R u_k^R + (p^L - p^R)], \tag{21}$$

and C is the acoustic impedance $C = \rho c$. The interface pressure $p^\star$ is:

$$p^\star = (1-\beta) p^{\star,incr} + \beta p^{\star,comp}. \tag{22}$$

In Eq. (22), the interface pressure is the sum of the incompressible and the compressible parts, where the incompressible contribution is:

$$p^{\star,incr} = \frac{C^L p^R + C^R p^L}{C^L + C^R}, \tag{23}$$

and the compressible contribution is:

$$p^{\star,comp} = \frac{C^L p^R + C^R p^L + C^R C^L (u_k^L - u_k^R)}{C^L + C^R} \tag{24}$$

Depending on the Mach number, the contribution of the incompressible or the compressible part in Eq. (22) is more dominant and the weighted term β is :

$$\beta = 1 - e^{-\alpha M}, \tag{25}$$

where the Mach number M is defined as:

$$M = max\Big(\frac{|\mathbf{u}^L|}{c^L}, \frac{|\mathbf{u}^R|}{c^R}\Big). \tag{26}$$

The blending coefficient is $\alpha \sim (10, 100)$. For incompressible single phase flow, Eq. (23) is taking the form of $\frac{1}{2}(p_L + p_R)$ since $C^L = C^R$. However, for two-phase flows, Eq. (23) is much closer to the exact solution.

Linear interpolation (2nd order spatial accuracy) with van Leer flux limiter has been used [124]. A four stage Runge-Kutta (RK), 4^{th} order accurate in time has been implemented for time advancement [122], in order to capture the waves which are propagating in the domain.

4. Results

In this section, verification and validation of the numerical method is performed; then, the effect of various impact velocities on a 2-D axisymmetric drop impact is investigated. The Riemann problem is chosen for verifying the algorithm accuracy and demonstrating its ability to resolve wave dynamics. Possible difficulties of the numerical scheme, which is prone to numerical diffusion and dispersion, especially at the phase boundaries are also investigated. The 2-D planar drop impact case is then selected for qualitative validation of the propagating shock and the reflected expansion waves against available experimental data. Finally, the 2-D axisymmetric drop impingement on a solid wall is modelled for different impact velocities, in order to investigate the extent of the cavitation zone and how bubble collapse can possibly lead to material erosion. The drop impact simulations are summarised in Table 1, where the Reynolds, Weber and Froude numbers are calculated.

4.1. Riemann Problem

The first benchmark case is the Riemann problem in the computational domain $x \in [-0.5, 0.5]$ with initial conditions for the left state: $\rho_L = 998.2\, kg/m^3$, $u_L = 0\, m/s$, $Y_g = 0$ and for the right state: $\rho_R = 0.017\, kg/m^3$, $u_R = 0\, m/s$, $Y_g = 1$. Wave transmissive boundary conditions have been used for the left and the right sides of the shock tube, that is $\mathbf{U}_{n+1}(x = L) = \mathbf{U}_n(x = L)$ and $\mathbf{U}_{n+1}(x = 0) = \mathbf{U}_n(x = 0)$. A CFL number of 0.5 was chosen for the time

Table 1: Numbering, description, impact velocity, Reynolds, Weber and Froude numbers of the drop impact cases which have been simulated. As wedge are denoted the 2-D axisymmetric simulations and no air means that in the initial condition the drop is attached to the wall, in comparison to the rest of the simulations where the drop is 3 cells above the wall in the beginning of the simulation.

Name	Description	u_{imp} (m/s)	Re	We	Fr
1	planar 2-D	110	$1.1 \cdot 10^6$	$1.67 \cdot 10^6$	351.2
2	wedge	110	$1.1 \cdot 10^6$	$1.67 \cdot 10^6$	351.2
3	wedge	27.5	$2.75 \cdot 10^5$	$1.05 \cdot 10^5$	87.8
4	wedge	55	$5.5 \cdot 10^5$	$4.19 \cdot 10^5$	175.6
5	wedge	82.5	$8.2 \cdot 10^5$	$9.43 \cdot 10^5$	263.4
6	wedge	220	$2.2 \cdot 10^6$	$6.71 \cdot 10^6$	702.4
7	wedge	550	$5.5 \cdot 10^6$	$4.19 \cdot 10^7$	1756
8	wedge, no air	27.5	$2.75 \cdot 10^5$	$1.05 \cdot 10^5$	87.8

step selection in the explicit algorithm. Comparison between the exact and the numerical solution is shown in Fig. 1 at time $t = 0.1\,\mu s$, where second order of spatial accuracy with 500 equally spaced cells in the x direction was used for obtaining the numerical solution. A close-up view in order to compare first and second order in space schemes with resolution either 500 or 1000 equally spaced cells in the x direction is shown in Fig. 2. In Fig. 1, the exact solution of the Riemann problem and the computed one are in satisfactory agreement and the wave pattern has been correctly captured. As it was expected in Fig. 2, the 2nd order solutions in space have minimal numerical diffusion, which is dominant in the 1st order schemes. In addition, the computed solution is getting closer to the exact by increasing the mesh resolution and the numerical diffusion is eliminated. No dispersion is noticed at the boundary interface (between the gas and the liquid), which is the case when using conventional schemes such as HLLC or similar. The exact solution of the Riemann problem is not trivial for multi-material cases and it has been derived following the Appendix A of the present paper.

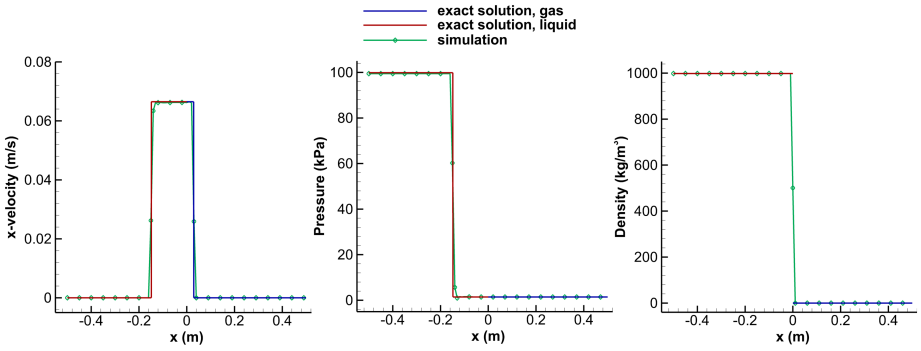

Figure 1: Verification of the two-phase solver in the Riemann problem. Comparison of the x-velocity (left), pressure (middle) and density (right) between the exact and the numerical solution at time $t = 0.1 \quad \mu s$. Second order accuracy in space with 500 cells has been used.

4.2. Planar drop impact

The second test case examined is a planar 'drop' impact on a solid wall for which experimental data are available [12]. A 2-D simulation, with second order discretization in space has been performed in order to validate the algorithm against the 2-D experimental data of Field at al. [12]. In the experimental apparatus of [12], a small quantity of liquid was placed between two transparent plates, separated by a small distance. Due to surface tension, the liquid formed a circular area of diameter $D = 10\,mm$; the distance between the two plates is negligible compared to the diameter D. The impact was modelled by a third plate which was projected with velocity $110\,m/s$ among the two plates. In the numerical simulation, the water drop ($Y = 0$) and the surrounding air ($Y = 1$) were set as initial conditions in the transport equation for the gas mass fraction. Therefore, the centre of the drop was placed at $(x_0, y_0) = (0, 0.00505)\,m$ in the computational domain $(-0.2, 0.2) \times (0, 0.2)\,m$; 150 cells have been placed along the initial drop radius R (grid size $\sim 33\,\mu m$). The same cell size as in the drop radius has been kept until distance $2R$ in the positive and negative x-direction and until $1.5R$ in the positive y-direction. After that, a stretching ratio of 1.05 has been applied, resulting in a total amount of $380\,k$ cells (see the left image of Fig. 3). A CFL number of 0.5 was chosen for the time step selection ($\Delta t \sim$

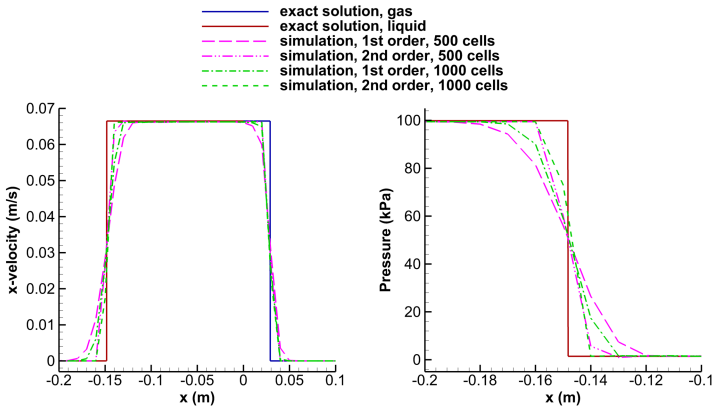

Figure 2: Close-up view of the Riemann problem. Comparison of the x-velocity (left) and pressure (right) between the exact and the numerical solution at time $t = 0.1\,\mu s$. First and second order spatial accuracy schemes with resolution of 500 and 1000 cells have been used.

$5 \cdot 10^{-9}\,s$) in the explicit algorithm. Initially, the pressure of the surrounding air and the water drop is atmospheric, $p(t = 0) = 101326\,Pa$. In this way, the initial density for the two phases is calculated from the barotropic EoS: $\rho_l(t = 0) = 998.207\,kg/m^3$ and $\rho_g(t = 0) = 1.204\,kg/m^3$. Zero gradient boundary conditions have been selected for the right, left and upper faces, whereas the lower face is set as wall. In Fig. 4 the experiment [12] (left) and the numerical solution (right) for the drop impact are compared.

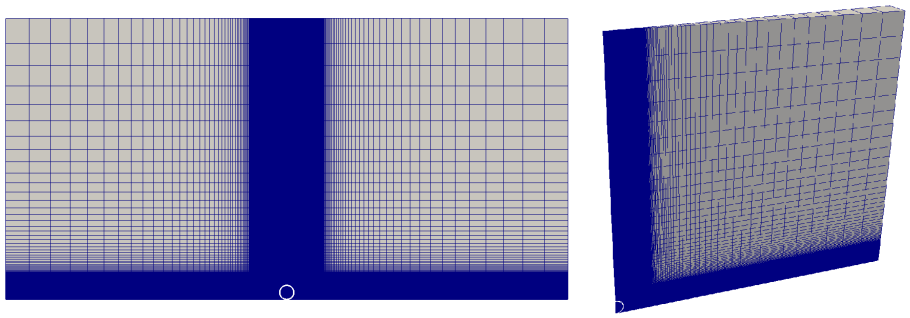

Figure 3: Computational grids for the planer drop impact (left) and for the 2-D axisymmetric drop impact (right).

The main mechanisms noticed both in the experimental work [10, 12] and past numerical simulations [102, 104, 105] are jetting, as well as shock and expansion waves; these are also identified in the present study. In the aforementioned compressible numerical studies, cavitation was not modelled and different impact conditions were simulated compared to the present work. In frame *(a)* the drop impacts the wall, whereas in the next frame, a shock wave is forming, as a result of the impact. While the liquid close to the impact point is compressed, the information of the impact has not travelled in the rest of the drop, which is still moving with the impact velocity [100]. Those two regions are separated by the shock front (frame *(b)*), which is created by individual wavelets emanating from the contact edge [101, 10]. In the preliminary stages of the impact, the edge velocity is higher than the speed of sound and there is a tendency to decrease. As long as the edge velocity is higher than the shock speed, the shock is attached to the contact edge. When the edge velocity reaches the critical value of the shock speed, the shock wave is detached from the contact line (frame *(c)*) and it is propagating in the rest of the liquid (until frame *(g)*). This mechanism is responsible for the expansion of the liquid and the jetting, which is created in the contact edge (frame *(d)*, denoted as J in the experimental results). In frames *(e)*, *(f)* and *(g)*, the shock wave is reflected normal to the free surface as an expansion wave which focuses in the inner region of the drop. These low pressure areas are potential cavitation regimes and their extent, as well as the volume of the vapour depend on the impact velocity [105]. In frames *(g)*, *(h)*, the shock wave reaches the highest point of the drop and it is then reflected downwards. In the last frames, the jetting is more advanced and the reflected shock is shown in the upper middle of the drop at frames *(i)* and *(j)* (denoted as R in frame *(i)* and focused to point F in frame *(j)* of the experiment).

Comparing the present simulation with previous experimental studies of Field et al. [12], similar wave structures at the same time scale are noticed. The edge pressure in the contact edge is around $0.22\,GPa$ and it exceeds the water hammer pressure [10], which is estimated about $0.16\,GPa$, where the water hammer pressure is defined as $p_{wh} = \rho_l c_l u_{imp}$. The shock wave moving

upwards and its reflection have been recognized at similar time frames between the experiment and the simulation. Furthermore, the jetting (starting from frame *(d)*) is around ten times the impact speed, or even higher, as it has been mentioned in [10]. Rarefaction waves have been also identified in the later stages of the drop impact and they follow the same pattern as in the experimental study. The production of vapour in the final stages is evident due to the pressure drop and the areas where vapour is generated are in accordance to the experiment. However, in the experimental study the maximum volume of vapour is in the centre of the drop, whereas in the present work, vapour is more dominant on the upper sides, perimetrically of the drop. This is because the bulk liquid tension cannot be captured with the present methodology.

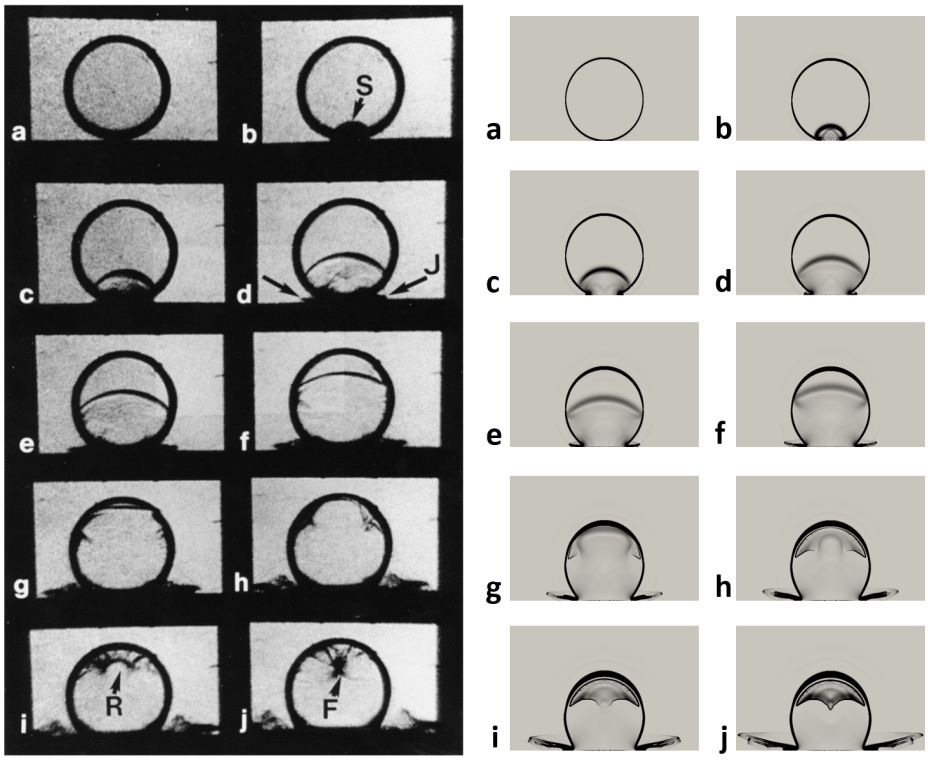

Figure 4: Validation of the numerical solution (right) against experiment (left) for a 2-D drop impact on a solid wall with impact velocity $110\,m/s$. The interframe time is $t = 1\,\mu s$. The left figure is taken from Field et. al [12].

4.3. 2-D axisymmetric drop impact

The previous simulation is now performed in a 2-D axisymmetric computational domain, in order to model the impact of spherical drops. A 3-D simulation would generally capture the 3-D interfacial instabilities due to surface tension, but since the We number is above 10^5 and in order to reduce the computational cost, a 2-D axisymmetric simulation is performed instead. The drop impact time scale is $t_{impact} = D/u_{imp}$ and in the present configuration for impact velocity $u_{imp} = 110\,m/s$ is calculated to be $t_{impact} \approx 9 \cdot 10^{-5}\,s$, whereas the cavitation collapse time is approximated from the characteristic Rayleigh time $t_{cav} = 0.915 R_{0,vap}\sqrt{\frac{\rho_l}{p_\infty - p_{sat}}}$ and it is calculated to be $t_{cav} \approx 2.2 \cdot 10^{-5}\,s$. Starting from the half of the 2-D meshes of 4.2, a wedge of 5 degrees has been simulated by taking advantage of the axial symmetry (see the right image of Fig. 3). The same initial and boundary conditions are kept, apart from the wedge faces and the axis of symmetry. At the beginning, a grid independence analysis is performed and then, the effect of the impact velocity magnitude is investigated for the intermediate grid. Second order accurate spatial discretization schemes have been used for this simulation and a CFL number of 0.5 was chosen for the time step selection ($\Delta t \sim 3 \cdot 10^{-10}\,s$) in the explicit algorithm. In the following figures, pressure has been non-dimensionalized with the water hammer pressure p_{wh}, velocity with the impact velocity u_{imp} and the dimensionless time is calculated from: $t = \frac{T - t_{bimp}}{D/c_l}$, where $t_{bimp} = 0.00005/u_{imp}$ is the time of the impact, based on the initial configuration (in cases where the drop is not attached to the wall, but there is air between them). This way, the shock wave will be at the same y-position at a given non-dimensional time for all impact velocities.

In Fig. 5 the results of the grid independence study are shown, for an impact velocity of $110\,m/s$. Three different grids have been utilized, with $117\,k$, $380\,k$ and $1.5\,M$ cells. In the fine area: $(0, 2R) \times (0, 1.5R)$ the resolution of 330×225, 660×450 and 1320×900 cells has been used for the three different grids. On the left-hand side of Fig. 5, the maximum wall pressure with respect to time is shown and on the right-hand side the generated volume of vapour at a line

parallel to the y axis ($x = 0.6\,mm$) at time $t = 1.19$ is plotted. The maximum wall pressures are similar for all grids and the peak noticed in the vapour volume fraction after $y = 0.8$ is almost identical for all resolutions. It can be concluded from the above study that there is convergence of the solution for the selected grid resolutions. The intermediate grid ($380\,k$ cells), referred as *case 2* from now on, is considered to be accurate enough and it is selected for the rest of the simulations.

In Fig. 6 and 7 the evolution of the drop impact is shown for *case 2*. More specifically, in Fig. 6 the pressure field (left half) and the velocity magnitude (right half) are shown in conjunction with the iso-surface of 0.5 gas mass fraction on the left figures; whereas on the right figures, the numerical Schlieren is depicted by utilizing different scales for the inner and the outer computational domain of the drop in order to capture the different waves, which are propagating in the liquid water and in the air. In Fig. 7 the wall pressure (lower part) and the vapour volume fraction (upper part) combined with the iso-surface of 0.5 gas mass fraction are demonstrated for *case 2*. The main mechanisms and the flow pattern in the 2-D axisymmetric simulation (*case 2*) are similar to the planar one (*case 1*) for the same impact velocity ($110\,m/s$). At time $t = 0.44$ the drop has already impacted the wall and the shock wave is visible in the Schlieren figure. The jetting has started, however it is more evident at time $t = 0.89$ and it is responsible for the non-spherical shape of the drop. As the shock moves to the upper half of the drop, it is reflected on the drop surface and expansion waves, which are moving downwards, are noticed in the Schlieren figures, starting from time $t = 0.89$. Those rarefaction waves create low pressure areas and thus, cavitation is noticed at times $t = 1.19$ and $t = 1.48$ (see also Fig. 7). The maximum wall pressure is realised at the moment of the impact and it decreases afterwards (see Fig. 12).

The planar and the axisymmetric solutions exhibit many similarities; nevertheless, there is a discrepancy in the pressure field between *case 1* and *case 2*. The maximum wall pressure is higher in *case 1*, as it can be seen in Fig. 8 and has been also noticed in previous studies [10]. In *case 1* the shock wave propa-

gates in a cylindrical pattern and it is reflected on the upper half surface of the cylinder, whereas in *case 2* the shock wave travels in a spherical pattern and it is reflected on the upper surface of the spherical drop. The three-dimensionality of the latter results in a shock wave of the half pressure strength ($\sim 10\,MPa$), compared to the planar case ($\sim 20\,MPa$).

In Fig. 9, the above results are compared to lower impact velocities, $55\,m/s$ and $27.5\,m/s$ at the same dimensionless time $t = 1.48$. The same configuration as in the left image of Fig. 6 is followed here as well. The drop spreading at lower impact speeds is less dominant and the drop is closer to the spherical shape, as it can be seen from the drop iso-surface plots. On the other hand, in *case 2* the transition to splashing is evident, as the jetting area is split to two different regions. Furthermore, the high pressure area and the lamella are larger in *case 2* but the ratio $|\mathbf{u}_{max}|/u_{imp}$ in all cases (*case 2-4*) is between 7.2 and 11, whereas the ratio p_{max}/p_{wh} is around 0.13. Although the above indicate similar non-dimensional maximum pressures and jetting velocities regardless the impact velocity, it is worth pointing out that the maximum pressure and velocity fields are significantly lower in *case 3* and *4*. For example, the jetting velocity is reduced by even one order of magnitude ($\sim$1400 m/s in *case 2* and $\sim$190 m/s in *case 4*).

In order to compare the vapour generated for each impact velocity at the same non dimensional time $t = 1.48$, slices with the vapour volume contour (upper) combined with the same iso-surface are shown in Fig. 10 for *case 2, 3* and *4*. For the highest impact velocity (*case 2*) the vapour volume is increased even one order of magnitude compared to the values of lower velocities. It can be concluded that the amount of the vapour and the extent of the cavitation area, which is generated at later stages, monotonically depends on the impact velocity (this is also evident in Fig. 12 where 6 different impact velocities are examined). The wall pressure (bottom) is also depicted in Fig. 10; although the maximum is approximately the same for all cases, it extends to a larger area for higher impact velocities.

At a later stage of the drop impact (Fig. 11), the splashing is more evident

than at time $t = 1.48$. In Fig. 11 the pressure field (left slice) and the velocity magnitude (right slice) are shown in conjunction with the iso-surface of 0.5 gas mass fraction on the left figures, whereas on the right figures the wall pressure (lower slice) and the vapour volume fraction (upper slice) combined with the iso-surface of 0.5 gas mass fraction are demonstrated for *case 2*. Several vaporous regions have been created from the rarefaction waves and they start collapsing consecutively. At times $t = 3.19$ and $t = 3.56$ the third and second vaporous regions have just collapsed respectively. A peak in the pressure due to the shock wave created by the collapse is noticed at times $t = 3.56$ and $t = 3.64$, however the location (far away from the wall) and the strength (maximum pressure is $0.09p_{wh}$) cannot denote erosion.

In Fig. 12 a parametric study for six different impact velocities (*case 2-7*) is performed for the intermediate grid resolution, where the maximum wall pressure (left) and the generated volume of vapour (right) with respect to time are plotted. As it has been already discussed in the previous paragraph and in previous studies [7, 105], it is straightforward that higher impact velocities result in higher wall pressures (although the ratio $\frac{p_{max,wall}}{p_{wh}}$ is almost constant regardless of the impact velocity). More production of vapour due to the reflection of a stronger shock developing during the liquid-solid contact is calculated. The cavitation inside the drop may also contribute to pressure increase on the solid surface at the bubble collapse stage. This is shown on the wall pressure figure, where at higher impact velocities there are small peaks occurring at later times (*case 7*).

It is remarkable that the initial configuration can affect the existence or not of cavitation and material erosion close to the wall, even for low impact velocities. As initial condition in *case 8* is now selected the drop to be attached to the wall (in contrast to *case 1-7*), so there is no air between them. To demonstrate that the impact velocity is not the determining factor here, $u_{imp} = 27.5\, m/s$ was selected. Surprisingly enough, in Fig. 13 vapour is created at the impact point and a vaporous region is formed above it due to a rarefaction wave at an early stage of the impact. The maximum vapour volume fraction created is even three

times higher than *case 2* at time $t = 1.48$, where the impact velocity is four times larger. Consequently, there is a significant increase in the pressure field due to the collapse, as it can be observed in Fig. 14, which results in around 60% higher wall pressure, compared to *case 3*. In practice, the above case can be realised at steam turbine blades, where the rarefied environment implies very low steam density, consequently there is little drop/vapour interaction.

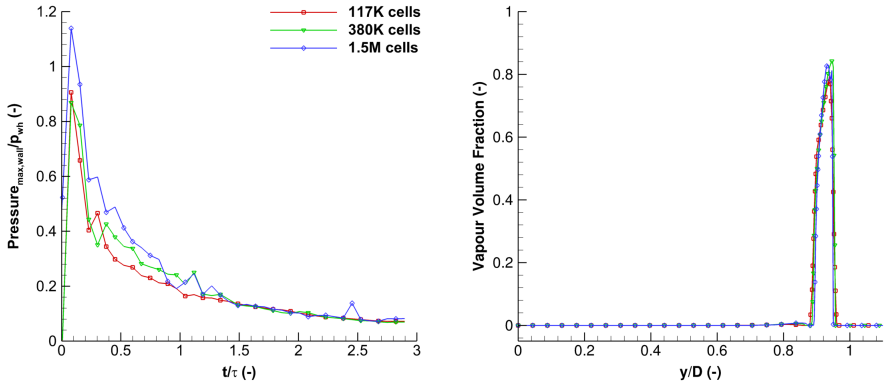

Figure 5: Grid independence study for three different grids (coarse, intermediate, fine). Maximum wall pressure with respect to time is shown on the left. The values of the vapour volume fraction on the right figure are exported at a line parallel to the y axis starting from $x = 0.6\,mm$, $z = 0$ at time $T = 0.083$. Wall pressure is divided by p_{wh}, time is measured from the moment of the impact and it is non-dimensionalized with $\tau = D/c_l$, whereas distance y has been divided by the drop diameter D.

5. Conclusions

In the present work, the impact of drops onto solid surfaces at conditions inducing cavitation within its volume have been addressed. Initially, a literature review on the subject has been given, focusing primarily on computational studies. It is apparent that the vast majority of them assume incompressible liquids and aim to resolve the temporal development of the drop/gas interface. Studies that consider the heat transfer and phase-change phenomena induced during impact at elevated wall temperature as well as wettability effects have

not been addressed here. However, more relevant to the present study are the conditions at high impact velocities where liquid compressibility becomes important. For conditions inducing cavitation within the drop's volume, only one set of experiments is reported in the literature while no computational study has been performed so far. Aiming to provide further inside to this problem, an explicit density-based solver of the Euler equations, able to model the co-existence of non-condensable gases, liquid and vapour phases has been developed and implemented in OpenFOAM. Moreover, a Mach number consistent numerical flux, capable of handling a wide range of Mach number flows and producing smooth solutions at the phase boundaries has been proposed. The main model assumptions and simplifications have been justified for the flow conditions of interest to the present study. The developed algorithm was then validated against the Riemann problem, followed by the comparison against the 2-D planar 'drop' impact experiment, showing satisfactory agreement, as similar flow patterns have been identified. Following, simulation of the impact of spherical drops on a solid surface have been performed, including for the first time the simulation of cavitation formation and collapse. These cavitation regimes are formed by the reflection of the shock wave on the outer surface of the drop as an expansion wave.

The drop impact time scale is $t_{impact} = D/u_{imp}$ and in the present configuration for impact velocity $u_{imp} = 110\,m/s$ is calculated to be $t_{impact} \approx 9 \cdot 10^{-5}\,s$, whereas the cavitation collapse time is approximated from the characteristic Rayleigh time $t_{cav} = 0.915 R_{0,vap}\sqrt{\frac{\rho_l}{p_\infty - p_{sat}}}$ and it is calculated to be $t_{cav} \approx 2.2 \cdot 10^{-5}\,s$. The significantly larger time scale ($t_{impact} \approx 9 \cdot 10^{-5}\,s$) of the drop impact phenomenon in comparison to the characteristic time of the cavitation collapse ($t_{cav} \approx 2.2 \cdot 10^{-5}\,s$) justifies why the collapse of the vaporous regions inside the drop don't affect the shape of the drop and its splashing. Increased impact velocity may result in more damage and possibly material erosion not only because of higher impact pressure, but also due to the collapse of the vaporous bubbles inside the drop. It is found that the initial location of the drop with respect to the solid surface, which actually means the absence or not of

gas around the drop, can influence the volume of cavitation generated at the initial stages of the impact. If there is no gas between the drop and the solid surface, pressure can get close to its maximum value, which is at the moment of the impact (p_{wh}) and material erosion may take place ($p_{wh} = 160\,MPa$ for $u_{imp} = 110\,m/s$ and the yield strength of steel is $200 - 300\,MPa$). It should be clarified here that the above phenomenon can even occur at low impact velocities, for instance at impact velocity $u_{imp} = 27.5\,m/s$.

Acknowledgements

The research leading to these results has received funding from the MSCA-ITN-ETN of the European Union's H2020 programme, under REA grant agreement n. 642536. The authors would also like to acknowledge the contribution of The Lloyd's Register Foundation. Lloyd's Register Foundation helps to protect life and property by supporting engineering-related education, public engagement and the application of research.

Appendix A. Exact Riemann problem for multi-material problems

In this section, the methodology for finding the exact solution to the Riemann problem for the multi-material Euler equations is derived. In the literature there are limited works discussing exact Riemann solvers for multi-material applications. Mainly, these focus on multiple velocities, pressures and temperature fields, see e.g. [125, 126]. The discussion here will be limited to just two different materials sharing the same velocity, pressure and temperature fields. The materials will be referred to as *material-1* and *material-2*, however the methodology may be extended to any number of materials. For the sake of generality, the discussion will not be limited to an explicit form of equation of state. Instead, the equations of state for the two distinct materials will be assumed to depend on density and internal energy only, i.e. have a form $p = p(\rho)$ or $p = p(\rho, e)$, which may have an explicit formula or be in tabular form as in [127, 96]. Material variation will be tracked using a mass fraction transport equation which

will affect the mixture equation of state. Thus, the mixture equation of state that will be examined is of the form $p = p(\rho, Y)$ or $p = p(\rho, e, Y)$, where Y is the mass fraction of *material-2*, defined in Eq. (9). Following Toro [122], the form of the Riemann problem solved is:

$$\begin{cases} \frac{\partial \mathbf{U}}{\partial t} + \frac{\partial \mathbf{F}(\mathbf{U})}{\partial x} = 0 \\ \mathbf{U}(x,0) = \begin{cases} \mathbf{U_L}, & \mathbf{x < 0} \\ \mathbf{U_R}, & \mathbf{x \geq 0} \end{cases} \end{cases} \tag{A.1}$$

The same nomenclature as in the rest of the paper is used.

Appendix A.1. Pressure is only a function of density and mass fraction

In case the mixture pressure is only a function of density and mass fraction, $p = p(\rho, Y)$ the conservative variables and the flux vector are:

$$\mathbf{U} = \begin{bmatrix} \rho \\ \rho u \\ \rho Y \end{bmatrix}, \quad \mathbf{F}(\mathbf{U}) = \begin{bmatrix} \rho u \\ \rho u^2 + p \\ \rho u Y \end{bmatrix}, \tag{A.2}$$

To derive the Jacobian matrix, it is convenient to recast the $\mathbf{U}$ and $\mathbf{F}(\mathbf{U})$ vectors and equation of state $p = p(\rho, Y)$, as:

$$\mathbf{U} = \begin{bmatrix} u_1 \\ u_2 \\ u_3 \end{bmatrix}, \quad \mathbf{F}(\mathbf{U}) = \begin{bmatrix} u_2 \\ \frac{u_2^2}{u_1} + p\left(u_1, \frac{u_3}{u_1}\right) \\ \frac{u_3 u_2}{u_1} \end{bmatrix}, \tag{A.3}$$

$$p = p\left(u_1, \frac{u_3}{u_1}\right) \tag{A.4}$$

The Jacobian matrix is calculated as:

$$\mathbf{A}(\mathbf{U}) = \begin{bmatrix} \frac{\partial f_1}{\partial u_1} & \frac{\partial f_1}{\partial u_2} & \frac{\partial f_1}{\partial u_3} \\ \frac{\partial f_2}{\partial u_1} & \frac{\partial f_2}{\partial u_2} & \frac{\partial f_2}{\partial u_3} \\ \frac{\partial f_3}{\partial u_1} & \frac{\partial f_3}{\partial u_2} & \frac{\partial f_3}{\partial u_3} \end{bmatrix} \tag{A.5}$$

After calculating all terms and replacing back the conservative variables:

$$\mathbf{A}(\mathbf{U}) = \begin{bmatrix} 0 & 1 & 0 \\ \frac{\partial p}{\partial \rho} - u^2 - \frac{\partial p}{\partial Y}\frac{Y}{\rho} & 2u & \frac{1}{\rho}\frac{\partial p}{\partial Y} \\ -uY & Y & u \end{bmatrix} \tag{A.6}$$

The eigenvalue analysis of the Jacobian matrix results to:

$$\begin{aligned} \lambda_1 &= u - c \\ \lambda_2 &= u \\ \lambda_3 &= u + c \end{aligned} \tag{A.7}$$

and right eigenvectors:

$$\mathbf{K_1} = \begin{bmatrix} 1 \\ u - c \\ Y \end{bmatrix}, \quad \mathbf{K_2} = \begin{bmatrix} \frac{\partial p}{\partial Y} \\ u\frac{\partial p}{\partial Y} \\ Y\frac{\partial p}{\partial Y} - \rho\frac{\partial p}{\partial \rho} \end{bmatrix}, \quad \mathbf{K_3} = \begin{bmatrix} 1 \\ u + c \\ Y \end{bmatrix} \tag{A.8}$$

where c is the speed of sound equal to $\sqrt{\frac{\partial p}{\partial \rho}}$. The waves associated with λ_1, λ_3 eigenvalues are non-linear waves (shock waves or rarefaction waves) and the λ_2 eigenvalue is a linearly degenerate wave associated with a contact discontinuity.

Appendix A.2. Pressure is a function of density, internal energy and mass fraction

In case the mixture pressure is only a function of density, internal energy and mass fraction, $p = p(\rho, e, Y)$ the conservative variables and the flux vector are:

$$\mathbf{U} = \begin{bmatrix} \rho \\ \rho u \\ \rho E \\ \rho Y \end{bmatrix}, \quad \mathbf{F}(\mathbf{U}) = \begin{bmatrix} \rho u \\ \rho u^2 + p \\ u(\rho E + p) \\ \rho u Y \end{bmatrix}, \tag{A.9}$$

where $E = 1/2u^2 + e$, with e the internal energy. To derive the Jacobian matrix, it is convenient to recast the $\mathbf{U}$ and $\mathbf{F}(\mathbf{U})$ vectors and EoS $p = p(\rho, e, Y)$ as:

$$\mathbf{U} = \begin{bmatrix} u_1 \\ u_2 \\ u_3 \\ u_4 \end{bmatrix}, \quad \mathbf{F}(\mathbf{U}) = \begin{bmatrix} u_2 \\ \frac{u_2^2}{u_1} + p\left(u_1, \frac{u_3}{u_1} - \frac{u_2^2}{2u_1}, \frac{u_4}{u_1}\right) \\ \frac{u_2}{u_1}\left(u_3 + p\left(u_1, \frac{u_3}{u_1} - \frac{u_2^2}{2u_1}, \frac{u_4}{u_1}\right)\right) \\ \frac{u_4 u_2}{u_1} \end{bmatrix}, \tag{A.10}$$

$$p = p\left(u_1, \frac{u_3}{u_1} - \frac{u_2^2}{2u_1}, \frac{u_4}{u_1}\right) \tag{A.11}$$

The Jacobian matrix is:

$$\mathbf{A}(\mathbf{U}) = \begin{bmatrix} 0 & 1 & 0 & 0 \\ \frac{2\frac{\partial p}{\partial \rho}\rho + \frac{\partial p}{\partial e}(u^2-2e) - 2\left(\rho u^2 + \frac{\partial p}{\partial Y}Y\right)}{2\rho} & \left(2 - \frac{\partial p}{\partial e}\frac{1}{\rho}\right)u & \frac{\partial p}{\partial e}\frac{1}{\rho} & \frac{\partial p}{\partial Y}\frac{1}{\rho} \\ \frac{u\left(-\frac{\partial p}{\partial e}u^2 + \rho u^2 + 2\frac{\partial p}{\partial e}e + 2p - 2\rho\frac{\partial p}{\partial \rho} + 2e\rho + 2Y\frac{\partial p}{\partial Y}\right)}{2\rho} & \frac{\left(\rho - 2\frac{\partial p}{\partial e}\right)u^2 + 2p + 2e\rho}{2\rho} & \frac{u}{\rho}\left(\frac{\partial p}{\partial e} + \rho\right) & \frac{u}{\rho}\frac{\partial p}{\partial Y} \\ -uY & Y & 0 & u \end{bmatrix} \tag{A.12}$$

The Jacobian eigenvalues $[\lambda_1, \lambda_2, \lambda_3, \lambda_4]$ are:

$$\begin{aligned} \lambda_1 &= u - c \\ \lambda_2 = \lambda_3 &= u \\ \lambda_4 &= u + c \end{aligned} \tag{A.13}$$

and right eigenvectors:

$$\mathbf{K_1} = \begin{bmatrix} 1 \\ u - c \\ \frac{1}{2}\Big(u^2 - cu + 2p/\rho + 2e\Big) \\ Y \end{bmatrix}, \quad \mathbf{K_2} = \begin{bmatrix} 2\frac{1}{X}\frac{\partial p}{\partial Y} \\ 2\frac{u}{X}\frac{\partial p}{\partial Y} \\ 0 \\ 1 \end{bmatrix}, \quad \mathbf{K_3} = \begin{bmatrix} 2\frac{1}{X}\frac{\partial p}{\partial e} \\ 2\frac{u}{X}\frac{\partial p}{\partial e} \\ 1 \\ 0 \end{bmatrix}, \quad \mathbf{K_4} = \begin{bmatrix} 1 \\ u + c \\ \frac{1}{2}\Big(u^2 + cu + 2p/\rho + 2e\Big) \\ Y \end{bmatrix} \tag{A.14}$$

where c is the speed of sound, defined as: $c = \sqrt{\frac{\partial p}{\partial \rho} + \frac{\partial p}{\partial e}\frac{p}{\rho^2}}$ and $X = \frac{\partial p}{\partial e}u^2 + 2\frac{\partial p}{\partial e}e - 2\frac{\partial p}{\partial \rho}\rho + 2\frac{\partial p}{\partial Y}Y$.

The waves associated with λ_1, λ_4 eigenvalues are non-linear waves (shock waves or rarefaction waves) and the λ_2, λ_3 eigenvalues are linearly degenerate waves associated with a contact discontinuity.

Appendix A.3. Exact solver derivation

Despite the difference in the Jacobian matrix structure with respect to the single material, ideal gas Euler equations [122], the eigenstructure is very similar. In both cases (pressure is function of ρ, Y or pressure is a function of ρ, e, Y), the eigenvalues correspond to two non-linear waves and one contract discontinuity wave. In fact, since the material interface will travel at the contact discontinuity, allows to split the original multi-material Riemann problem, to two coupled single-material Riemann problems, as shown in Fig. A.15 and A.16.

Consequently, to solve the multi-material Riemann problem exactly, one has to do the following procedure:

- Assume an initial star region velocity, $u^\star$.

- Based on this assumed $u^\star$, solve each material separately, with a single material Riemann solver, assuming that the contact discontinuity is a moving wall at velocity $u_{wall} = u^\star$. General Riemann solvers for arbitrary equations of state in the form of $p = p(\rho)$ or $p = p(\rho, e)$ may be found in [96]. The solution of each single-material problem is done assuming wall boundary conditions, i.e. $p_R = p_L$, $\rho_R = \rho_L$, but $u_R = -u_L + 2u_{wall}$. For example, in Fig. A.16, when solving for *material-1*, the right state conditions are $\mathbf{U} = \begin{bmatrix} \rho_L & \rho_L(2u_{wall} - u_L) & e_L \end{bmatrix}^{\mathbf{T}}$. Similarly for *material-2*, the left state conditions are $\mathbf{U} = \begin{bmatrix} \rho_R & \rho_R(2u_{wall} - u_R) & e_R \end{bmatrix}^{\mathbf{T}}$.

- After solving the two individual Riemann problems for *material-1* and *material-2*, the calculated star region pressure for the two materials $p_1^\star$ and $p_2^\star$ is not necessarily the same. Thus, the u^* velocity must be corrected iteratively, until $p_1^\star = p_2^\star$.

- Once $p_1^\star = p_2^\star$ up to a prescribed tolerance, the exact solution of the Riemann problem is the superposition of the two individual problems, i.e. the L and L^* states from *material-1* and R and R^* states from *material-2*. Note that in cases of large disparities in the acoustic impedance of the materials (e.g. liquid/gas interfaces), $p^\star$ will be very sensitive to small variations of $u^\star$ for the stiff phase, thus under-relaxation of the corrected $u^\star$ is advised.

As a demonstration of the aforementioned solver, the following cases will be examined and compared with PVRS solvers in literature [122]. The material properties are as follows:

material-1: Liquid EoS, $p = c_L^2(\rho - \rho_{l,sat}) + p_{sat}$, $c_L = 1482.35\,m/s$, $p_{sat} = 2340\,Pa$, $\rho_{l,sat} = 998.16\,kg/m^3$

material-2: Gas EoS, $p = \rho R_g T_{ref}$, $R_g = 287.06\,J/(kgK)$, $T_{ref} = 293\,K$

Appendix A.3.1. Case A

The initial configuration of the Riemann problem is shown in Table A.2. The exact solution is $p^\star = 1430.9\,Pa$ and $u^\star = 0.067\,m/s$. The PVRS-solver, using average states between L, R fails to properly predict the star region; in fact, it

predicts $p^\star = 50666.7\,Pa$ (3440.9 % deviation from exact) and $u^\star = 0.11\,m/s$ (66.9 % deviation from exact). On the other hand, the PVRS-solver outlined in section 3.4, predicts $p^\star = 1430.9\,Pa$ (practically identical to exact solution) and $u^\star = 0.066\,m/s$ (0.2 % deviation from exact). Note that this is the same case used for validation in section 4.1.

Table A.2: Initial configuration for the Riemann problem of Appendix A.3.1.

material-1, $x < 0$ (Liquid)	*material-2*, $x \geq 0$ (Gas)
$\rho_L = 998.202\,kg/m^3$	$\rho_R = 0.017\,kg/m^3$
$u_L = 0\,m/s$	$u_R = 0\,m/s$
$p_L = 99902.8\,Pa$	$p_R = 1400\,Pa$

Appendix A.3.2. Case B

The second Riemann problem is a much more demanding case, since there is a huge pressure and density variation between the L, R states. The initial configuration of this Riemann problem is shown in Table A.3. The exact solution is $p^\star = 144.4\,Pa$ and $u^\star = 2.73\,m/s$. The PVRS-solver, using average states between L, R again fails to properly predict the star region, due to the averaging; in fact, it predicts $p^\star = 20.2 \cdot 10^5\,Pa$ (1400000 % deviation from exact) and $u^\star = 4.56\,m/s$ (66.7 % deviation from exact). On the other hand, the PVRS-solver outlined in section 3.4, predicts $p^\star = 144.4\,Pa$ (practically identical to exact solution) and $u^\star = 2.72\,m/s$ (0.32 % deviation from exact).

Table A.3: Initial configuration for the Riemann problem of Appendix A.3.2.

material-1, $x < 0$ (Liquid)	*material-2*, $x \geq 0$ (Gas)
$\rho_L = 1000\,kg/m^3$	$\rho_R = 0.0017\,kg/m^3$
$u_L = 0\,m/s$	$u_R = 0\,m/s$
$p_L = 40.4 \cdot 10^5\,Pa$	$p_R = 143\,Pa$

Appendix A.3.3. Case C

In this case, although the pressure and density ratios are much lower than the case in section Appendix A.3.2, the challenge is to predict the induced depressurization due to the high gas velocity. The initial configuration of this Riemann problem is shown in Table A.4. The exact solution is $p^\star = 81548\,Pa$ and $u^\star = 2.68\,m/s$. The PVRS-solver, using average states between L, R again fails catastrophically, predicting a negative $p^\star$; it predicts $p^\star = -154923\,Pa$ (290 % deviation from exact) and $u^\star = 9.46\,m/s$ (250 % deviation from exact). On the other hand, the PVRS-solver outlined in section 3.4, predicts $p^\star = 82025\,Pa$ (0.59 % deviation from exact solution) and $u^\star = 2.67\,m/s$ (0.33 % deviation from exact).

Table A.4: Initial configuration for the Riemann problem of Appendix A.3.3.

material-1, $x < 0$ (Liquid)	*material-2*, $x \geq 0$ (Gas)
$\rho_L = 1000\,kg/m^3$	$\rho_R = 1\,kg/m^3$
$u_L = 0\,m/s$	$u_R = 10\,m/s$
$p_L = 40.4 \cdot 10^5\,Pa$	$p_R = 84151\,Pa$

Appendix A.3.4. Case D

Also, in order to demonstrate the capability in predicting temperature effects and taking into account energy equation, a case examined by Saurel et al. [126] will be discussed. This case involves interaction of vapour and liquid dodecane, modelled as ideal gas and stiffened gas respectively. The properties of the materials are:

material-1: Liquid, stiffened gas EoS, $p = e(\gamma_L - 1)\rho - \gamma_L p_\infty$, $e = c_{v,L}T + \frac{p_\infty}{\rho}$, $c_{v,L} = 1077\,J/(kgK)$, $p_\infty = 4 \cdot 10^8\,Pa$, $\gamma_L = 2.35$

material-2: Ideal gas EoS, $p = \rho R_g T_{ref}$, $e = c_{v,G}T$, $R_g = 48.9\,J/(kgK)$, $c_{v,G} = 1956\,J/(kgK)$

The initial discontinuity in this case is described in Table A.5. The exact solution with the described solver is $p^\star = 186835.8\,kg/m^3$, $u^\star = 140.7\,m/s$, $\rho_{\star,L} =$

$454.9\,kg/m^3$, $\rho_{\star,R} = 3.68\,kg/m^3$ which is identical with the published solution.

Table A.5: Initial configuration for the Riemann problem of Appendix A.3.3.

material-1, $x < 0$ (Liquid)	*material-2*, $x \geq 0$ (Gas)
$\rho_L = 500\,kg/m^3$	$\rho_R = 2\,kg/m^3$
$u_L = 0\,m/s$	$u_R = 0\,m/s$
$p_L = 10^8\,Pa$	$p_R = 10^5\,Pa$
$T_L = 688\,k$	$T_R = 1022.3\,K$

Appendix B. Isentropic Compression

In Table B.6, isentropic compression of liquid water starting from saturation conditions ($T = 293\,K$, $p = 2317Pa$) is calculated based on the properties of [128, 129]. The temperature increase is negligible for pressure $2500\,bar$ ($\sim 6\,K$) and even for higher pressures, temperature increase is not significant in comparison to the other phenomena which take place. For example, in the previous drop simulations for impact velocity 110 m/s, the maximum pressure is $1460\,bar$ resulting in temperature increase less than $3.5\,K$. The above justify the barotropic EoS which was selected and the omission of thermal effects.

Table B.6: Temperature difference for isentropic compression of liquid water. Properties are derived from [128].

Pressure (Pa)	Temperature (K)	Temperature Difference (K)
2317.45	293	0
10^7	293.15	0.15
10^8	294.959	1.959
$2.5 \cdot 10^8$	299.109	6.109
$5 \cdot 10^8$	306.905	13.905
10^9	321.933	28.933

References

[1] M. Rein, Phenomena of liquid drop impact on solid and liquid surfaces, Fluid Dynamics Research 12 (1993) 61–93. doi:10.1016/0169-5983(93)90106-K.

[2] R. I. Crane, Droplet deposition in steam turbines, Proceedings of the Institution of Mechanical Engineers, Part C: Journal of Mechanical Engineering Science 218 (8) (2004) 859–870. arXiv:http://dx.doi.org/10.1243/0954406041474200, doi:10.1243/0954406041474200.
URL http://dx.doi.org/10.1243/0954406041474200

[3] A. L. Yarin, Drop impact dynamics: Splashing, spreading, receding, bouncing, Annual Review of Fluid Mechanics 38 (1) (2006) 159–192. arXiv:http://dx.doi.org/10.1146/annurev.fluid.38.050304.092144, doi:10.1146/annurev.fluid.38.050304.092144.
URL http://dx.doi.org/10.1146/annurev.fluid.38.050304.092144

[4] G. D. Martin, S. D. Hoath, I. M. Hutchings, Inkjet printing - the physics of manipulating liquid jets and drops, Journal of Physics: Conference Series 105 (1) (2008) 012001.
URL http://stacks.iop.org/1742-6596/105/i=1/a=012001

[5] R. Andrade, O. Skurtys, F. Osorio, Drop impact behavior on food using spray coating: Fundamentals and applications, Food Research International 54 (1) (2013) 397–405. doi:https://doi.org/10.1016/j.foodres.2013.07.042.
URL http://www.sciencedirect.com/science/article/pii/S0963996913004080

[6] A. L. Yarin, I. V. Roisman, C. Tropea, Collision Phenomena in Liquids and Solids, Cambridge University Press, 2017. doi:10.1017/9781316556580.

[7] J. Fukai, Z. Zhao, D. Poulikakos, C. M. Megaridis, O. Miyatake, Modeling of the deformation of a liquid droplet impinging upon a flat surface,

Physics of Fluids A: Fluid Dynamics 5 (11) (1993) 2588–2599. arXiv:http://dx.doi.org/10.1063/1.858724, doi:10.1063/1.858724.
URL http://dx.doi.org/10.1063/1.858724

[8] Y. Guo, Y. Lian, M. Sussman, Investigation of drop impact on dry and wet surfaces with consideration of surrounding air, Physics of Fluids 28 (7) (2016) 073303. arXiv:http://aip.scitation.org/doi/pdf/10.1063/1.4958694, doi:10.1063/1.4958694.
URL http://aip.scitation.org/doi/abs/10.1063/1.4958694

[9] Q. Zhou, N. Li, X. Chen, A. Yonezu, T. Xu, S. Hui, D. Zhang, Water drop erosion on turbine blades: Numerical framework and applications, MATERIALS TRANSACTIONS 49 (7) (2008) 1606–1615. doi:10.2320/matertrans.MRA2008025.

[10] J. E. Field, M. B. Lesser, J. P. Dear, Studies of two-dimensional liquid-wedge impact and their relevance to liquid-drop impact problems, Proceedings of the Royal Society of London A: Mathematical, Physical and Engineering Sciences 401 (1821) (1985) 225–249. doi:10.1098/rspa.1985.0096.
URL http://rspa.royalsocietypublishing.org/content/401/1821/225

[11] J. E. Field, J. P. Dear, J. E. Ogren, The effects of target compliance on liquid drop impact, Journal of Applied Physics 65 (2) (1989) 533–540. arXiv:http://dx.doi.org/10.1063/1.343136, doi:10.1063/1.343136.
URL http://dx.doi.org/10.1063/1.343136

[12] J. Field, J.-J. Camus, M. Tinguely, D. Obreschkow, M. Farhat, Cavitation in impacted drops and jets and the effect on erosion damage thresholds, Wear 290291 (2012) 154–160. doi:http://doi.org/10.1016/j.wear.2012.03.006.
URL http://www.sciencedirect.com/science/article/pii/S0043164812000968

[13] F. H. Harlow, J. P. Shannon, The splash of a liquid drop, Journal of Applied Physics 38 (10) (1967) 3855–3866. arXiv:http://dx.doi.org/10.1063/1.1709031, doi:10.1063/1.1709031.
URL http://dx.doi.org/10.1063/1.1709031

[14] C. Hirt, B. Nichols, Volume of fluid (VOF) method for the dynamics of free boundaries, Journal of Computational Physics 39 (1) (1981) 201–225. doi:http://dx.doi.org/10.1016/0021-9991(81)90145-5.
URL http://www.sciencedirect.com/science/article/pii/0021999181901455

[15] D. L. Youngs, An interface tracking method for a 3D Eulerian hydrodynamics code, Technical report 44/92/35, AWRE (1984).

[16] M. Rudman, Volume-tracking methods for interfacial flow calculations, International Journal for Numerical Methods in Fluids 24 (7) (1997) 671–691. doi:10.1002/(SICI)1097-0363(19970415)24:7<671::AID-FLD508>3.0.CO;2-9.
URL http://dx.doi.org/10.1002/(SICI)1097-0363(19970415)24:7<671::AID-FLD508>3.0.CO;2-9

[17] W. Aniszewski, T. Ménard, M. Marek, Volume of fluid (VOF) type advection methods in two-phase flow: A comparative study, Computers & Fluids 97 (2014) 52–73. doi:https://doi.org/10.1016/j.compfluid.2014.03.027.
URL http://www.sciencedirect.com/science/article/pii/S0045793014001261

[18] J. Fukai, Y. Shiiba, T. Yamamoto, O. Miyatake, D. Poulikakos, C. M. Megaridis, Z. Zhao, Wetting effects on the spreading of a liquid droplet colliding with a flat surface: Experiment and modeling, Physics of Fluids 7 (2) (1995) 236–247. arXiv:https://doi.org/10.1063/1.868622, doi:10.1063/1.868622.
URL https://doi.org/10.1063/1.868622

[19] M. Francois, W. Shyy, Computations of drop dynamics with the immersed boundary method, part 2: drop impact and heat transfer, Numerical Heat Transfer, Part B: Fundamentals 44 (2) (2003) 119–143. arXiv:https://doi.org/10.1080/713836348, doi:10.1080/713836348.
URL https://doi.org/10.1080/713836348

[20] Š. Šikalo, H.-D. Wilhelm, I. V. Roisman, S. Jakirlić, C. Tropea, Dynamic contact angle of spreading droplets: Experiments and simulations, Physics of Fluids 17 (6) (2005) 062103. arXiv:https://doi.org/10.1063/1.1928828, doi:10.1063/1.1928828.
URL https://doi.org/10.1063/1.1928828

[21] S. Mitra, M. J. Sathe, E. Doroodchi, R. Utikar, M. K. Shah, V. Pareek, J. B. Joshi, G. M. Evans, Droplet impact dynamics on a spherical particle, Chemical Engineering Science 100 (2013) 105–119, 11th International Conference on Gas-Liquid and Gas-Liquid-Solid Reactor Engineering. doi:https://doi.org/10.1016/j.ces.2013.01.037.
URL http://www.sciencedirect.com/science/article/pii/S000925091300050X

[22] M. Pasandideh-Fard, S. Aziz, S. Chandra, J. Mostaghimi, Cooling effectiveness of a water drop impinging on a hot surface, International Journal of Heat and Fluid Flow 22 (2) (2001) 201–210. doi:https://doi.org/10.1016/S0142-727X(00)00086-2.
URL http://www.sciencedirect.com/science/article/pii/S0142727X00000862

[23] M. Bussmann, J. Mostaghimi, S. Chandra, On a three-dimensional volume tracking model of droplet impact, Physics of Fluids 11 (6) (1999) 1406–1417. arXiv:http://dx.doi.org/10.1063/1.870005, doi:10.1063/1.870005.
URL http://dx.doi.org/10.1063/1.870005

[24] I. Roisman, L. Opfer, C. Tropea, M. Raessi, J. Mostaghimi,

S. Chandra, Drop impact onto a dry surface: Role of the dynamic contact angle, Colloids and Surfaces A: Physicochemical and Engineering Aspects 322 (1) (2008) 183–191. doi:https://doi.org/10.1016/j.colsurfa.2008.03.005.
URL http://www.sciencedirect.com/science/article/pii/S0927775708001738

[25] M. Marengo, C. Antonini, I. V. Roisman, C. Tropea, Drop collisions with simple and complex surfaces, Current Opinion in Colloid & Interface Science 16 (4) (2011) 292–302. doi:https://doi.org/10.1016/j.cocis.2011.06.009.
URL http://www.sciencedirect.com/science/article/pii/S1359029411000859

[26] A. M. Ardekani, S. Dabiri, R. H. Rangel, Deformation of a droplet in a particulate shear flow, Physics of Fluids 21 (9) (2009) 093302. arXiv:https://doi.org/10.1063/1.3205446, doi:10.1063/1.3205446.
URL https://doi.org/10.1063/1.3205446

[27] I. Malgarinos, N. Nikolopoulos, M. Gavaises, Numerical investigation of heavy fuel droplet-particle collisions in the injection zone of a fluid catalytic cracking reactor, part ii: 3d simulations, Fuel Processing Technology 156 (2017) 43–53. doi:https://doi.org/10.1016/j.fuproc.2016.09.012.
URL http://www.sciencedirect.com/science/article/pii/S0378382016305136

[28] B. J. Parker, D. L. Youngs, Two and three dimensional Eulerian simulation of fluid flow with material interfaces, Technical report, UK Atomic Weapons Establishment, Aldermaston, Berkshire (01/1992).

[29] R. Scardovelli, S. Zaleski, Direct numerical simulation of free-surface and interfacial flow, Annual Review of Fluid Mechanics 31 (1) (1999) 567–603. arXiv:https://doi.org/10.1146/annurev.fluid.31.1.567,

doi:10.1146/annurev.fluid.31.1.567.
URL https://doi.org/10.1146/annurev.fluid.31.1.567

[30] K. Yokoi, Efficient implementation of {THINC} scheme: A simple and practical smoothed {VOF} algorithm, Journal of Computational Physics 226 (2) (2007) 1985–2002. doi:https://doi.org/10.1016/j.jcp.2007.06.020.
URL http://www.sciencedirect.com/science/article/pii/S0021999107002732

[31] M. Marek, W. Aniszewski, A. Boguslawski, Simplified volume of fluid method (svof) for two-phase flows., TASK Quaterly 12 (2008) 25565.

[32] F. Xiao, Y. Honma, T. Kono, A simple algebraic interface capturing scheme using hyperbolic tangent function, International Journal for Numerical Methods in Fluids 48 (9) (2005) 1023–1040. doi:10.1002/fld.975.
URL http://dx.doi.org/10.1002/fld.975

[33] D. P. Garrick, W. A. Hagen, J. D. Regele, An interface capturing scheme for modeling atomization in compressible flows, Journal of Computational Physicsdoi:https://doi.org/10.1016/j.jcp.2017.04.079.
URL http://www.sciencedirect.com/science/article/pii/S0021999117303674

[34] F. Xiao, S. Ii, C. Chen, Revisit to the {THINC} scheme: A simple algebraic {VOF} algorithm, Journal of Computational Physics 230 (19) (2011) 7086–7092. doi:https://doi.org/10.1016/j.jcp.2011.06.012.
URL http://www.sciencedirect.com/science/article/pii/S0021999111003615

[35] R. K. Shukla, C. Pantano, J. B. Freund, An interface capturing method for the simulation of multi-phase compressible flows, Journal of Computational Physics 229 (19) (2010) 7411–7439.

doi:https://doi.org/10.1016/j.jcp.2010.06.025.
URL http://www.sciencedirect.com/science/article/pii/S0021999110003402

[36] M. L. Norman, K.-H. A. Winkler, 2-D Eulerian Hydrodynamics with Fluid Interfaces, Self-Gravity and Rotation, Springer Netherlands, Dordrecht, 1986, pp. 187–221. doi:10.1007/978-94-009-4754-2_6.
URL http://dx.doi.org/10.1007/978-94-009-4754-2_6

[37] E. Puckett, J. Saltzman, A 3d adaptive mesh refinement algorithm for multimaterial gas dynamics, Physica D: Nonlinear Phenomena 60 (1) (1992) 84 – 93. doi:http://dx.doi.org/10.1016/0167-2789(92)90228-F.
URL http://www.sciencedirect.com/science/article/pii/016727899290228F

[38] G. H. Miller, E. G. Puckett, A high-order godunov method for multiple condensed phases, Journal of Computational Physics 128 (1) (1996) 134–164. doi:http://dx.doi.org/10.1006/jcph.1996.0200.
URL http://www.sciencedirect.com/science/article/pii/S0021999196902004

[39] R. Saurel, R. Abgrall, A simple method for compressible multifluid flows, SIAM Journal on Scientific Computing 21 (3) (1999) 1115–1145.

[40] J. Roenby, H. Bredmose, H. Jasak, A computational method for sharp interface advection, Royal Society Open Science 3 (11). doi:10.1098/rsos.160405.
URL http://rsos.royalsocietypublishing.org/content/3/11/160405

[41] T. Marić, H. Marschall, D. Bothe, vofoam - a geometrical volume of fluid algorithm on arbitrary unstructured meshes with local dynamic adaptive mesh refinement using openfoam (arXiv:1305.3417). arXiv:1305.3417v1.

[42] S. Popinet, Gerris: a tree-based adaptive solver for the incompressible euler equations in complex geometries, Journal of Computational Physics 190 (2) (2003) 572–600. doi:https://doi.org/10.1016/S0021-9991(03)00298-5.
URL http://www.sciencedirect.com/science/article/pii/S0021999103002985

[43] D. Fuster, G. Agbaglah, C. Josserand, S. Popinet, S. Zaleski, Numerical simulation of droplets, bubbles and waves: state of the art, Fluid Dynamics Research 41 (6).
URL http://stacks.iop.org/1873-7005/41/i=6/a=065001

[44] M. S. Plesset, R. B. Chapman, Collapse of an initially spherical vapour cavity in the neighbourhood of a solid boundary, Journal of Fluid Mechanics 47 (1971) 283–290.

[45] W. Lauterborn, H. Bolle, Experimental investigations of cavitation-bubble collapse in the neighbourhood of a solid boundary, Journal of Fluid Mechanics 72 (2) (1975) 391–399. doi:10.1017/S0022112075003448.

[46] A. Philipp, W. Lauterborn, Cavitation erosion by single laser-produced bubbles, Journal of Fluid Mechanics 361 (1998) 75–116. doi:10.1017/S0022112098008738.

[47] I. Akhatov, O. Lindau, A. Topolnikov, R. Mettin, N. Vakhitova, W. Lauterborn, Collapse and rebound of a laser-induced cavitation bubble, Physics of Fluids 13 (10) (2001) 2805–2819. arXiv:https://doi.org/10.1063/1.1401810, doi:10.1063/1.1401810.
URL https://doi.org/10.1063/1.1401810

[48] S. Zhang, J. Duncan, G. Chahine, The final stage of the collapse of a cavitation bubble near a rigid wall, Journal of Fluid Mechanics 257 (1993) 147–181.

[49] S. Zhang, J. H. Duncan, G. L. Chahine, The behavior of a cavitation bubble near a rigid wall, in: J. R. Blake, J. M. Boulton-Stone, N. H. Thomas (Eds.), Bubble Dynamics and Interface Phenomena, Springer Netherlands, Dordrecht, 1994, pp. 429–436.

[50] A. M. Zhang, X. L. Yao, L. H. Feng, The dynamic behavior of a gas bubble near a wall 36 (2009) 295–305.

[51] L. Zhangrui, L. Sun, Z. Zong, Numerical analysis of gas bubbles in close proximity to a movable or deformable body 83 (2013) 1715–1737.

[52] G. A. Curtiss, D. M. Leppinen, Q. Wang, J. Blake, Ultrasonic cavitation near a tissue layer 730 (2013) 245–272.

[53] Z.-R. Li, L. Sun, Z. Zhi, J. Dong, A boundary element method for the simulation of non-spherical bubbles and the interactions near a free surface 28 (2012) 51–65.

[54] G. Tryggvason, R. Scardovelli, S. Zaleski, Direct Numerical Simulations of Gas-Liquid Multiphase Flows, Cambridge University Press, 2011.

[55] G. Chahine, Modeling of cavitation dynamics and interaction with material, in: K.-H. Kim, G. Chahine, J.-P. Franc, A. Karimi (Eds.), Advanced Experimental and Numerical Techniques for Cavitation Erosion Prediction, Springer, the Netherlands, 2014, pp. 123–161.

[56] N. A. Adams, S. J. Schmidt, Shocks in Cavitating Flows, in: F. C. Delale (Ed.), Bubble Dynamics and Shock Waves, Springer Berlin Heidelberg, Berlin, Heidelberg, 2013, pp. 235–256.

[57] F. Pöhl, S. Mottyll, R. Skoda, S. Huth, Evaluation of cavitation-induced pressure loads applied to material surfaces by finite-element-assisted pit analysis and numerical investigation of the elasto-plastic deformation of metalic materials 330-331 (2014) 618–628.

[58] D. Rossinelli, B. Hejazialhosseini, P. Hadjidoukas, C. Bekas, A. Curioni, A. Bertsch, S. Futral, S. J. Schmidt, N. A. Adams, P. Koumoutsakos, 11pflop/s simulations of cloud cavitation collapse, in: SC '13 Proceedings of the International Conference on High Performance Computing, Networking, Storage and Analysis, no. 3, ACM New York, Denver, CO, USA, 2013.

[59] B. B. Li, W. Jia, H. C. Zhang, J. Lu, Investigation on the collapse behavior of a cavitation bubble near a conical rigid boundary, Shock Waves 24 (2014) 317–324. doi:10.1007/s00193-013-0482-3.

[60] B. R. Shin, Numerical simulation of cavitation bubble collapse near wall, in: A. Kuzmin (Ed.), Computational Fluid Dynamics 2010, Springer-Verlag, Berlin Heidelberg, 2010, pp. 913–915.

[61] E. Johnsen, T. Colonius, Numerical simulations of non-spherical bubble collapse 629 (2009) 231–262.

[62] S. Nagrath, K. Jansen, R. Lahey, I. Akhatov, Hydrodynamic simulation of air bubble implosion using a level set approach 215 (2006) 98–132.

[63] E. Lauer, X. Y. Hu, S. Hickel, N. A. Adams, Numerical modelling and investigation of symmetric and asymmetric cavitation bubble dynamics, Computers & Fluids 69 (2012) 1–19. doi:http://dx.doi.org/10.1016/j.compfluid.2012.07.020.

[64] N. A. Hawker, Y. Ventikos, Shock/gas bubble interactions in infinite and finite volumes of liquid, in: 2nd Micro and Nano Flows Conference, West London, UK, 2009.

[65] E. Maitre, Review of the numerical methods for free interfaces, Tech. rep., Laboratoire mixte de l' Ecole Polytechnique et du CNRS (2006).

[66] S. Umemura, K. Kawabata K Fau Sasaki, K. Sasaki, In vivo acceleration of ultrasonic tissue heating by microbubble agent, IEEE Transactions on

Ultrasonics, Ferroelectrics, and Frequency Control 52 (10) (2005) 1690–1698. doi:10.1109/TUFFC.2005.1561623.

[67] J.-P. Franc, M. Riondet, A. Karimi, G. L. Chahine, Material and velocity effects on cavitation erosion pitting, Wear 274-275 (2012) 248–259. doi:https://doi.org/10.1016/j.wear.2011.09.006.
URL http://www.sciencedirect.com/science/article/pii/S0043164811005886

[68] G. Chahine, A. Kapahi, J.-K. Choi, C.-T. Hsiao, Modeling of surface cleaning by cavitation bubble dynamics and collapse, Ultrasonics Sonochemistry 29 (2016) 528–549. doi:https://doi.org/10.1016/j.ultsonch.2015.04.026.
URL http://www.sciencedirect.com/science/article/pii/S1350417715001194

[69] S. Hickel, M. Mihatsch, S. Schmidt, Implicit large eddy simulation of cavitation in micro channel flows, WIMRC 3rd International Cavitation Forum 2011, University of Warwick, UK, 2011.

[70] N. Berchiche, J.-P. Franc, J.-M. Michel, A cavitation erosion model for ductile materials, J. Fluids Eng 124 (2002) 601–606.

[71] R. F. Kunz, D. A. Boger, D. R. Stinebring, T. S. Chyczewski, J. W. Lindau, H. J. Gibeling, S. Venkateswaran, T. R. Govindan, A preconditioned navier-stokes method for two-phase flows with application to cavitation prediction, Computers & Fluids 29 (2000) 849–875. doi:https://doi.org/10.1016/S0045-7930(99)00039-0.

[72] W. S. Senocak, I., A pressure-based method for turbulent cavitating flow computations, Journal of Computational Physics 176(2) (2002) 363–383.

[73] A. Alajbegovic, H. A. Grogger, H. Philipp, Calculation of transient cavitation in nozzle using the two-fluid model, in: 12th ILASS-America, USA, 1999.

[74] G. H. Schnerr, J. Sauer, Physical and numerical modeling of unsteady cavitation dynamics, in: ICMF 2001, 4th Int. Conf. on Multiphase Flows, New Orleans, USA, 2001.

[75] A. K. Singhal, M. M. Athavale, H. Li, Y. Jiang, Mathematical basis and validation of the full cavitation model, Journal of Fluids Engineering 124 (3) (2002) 617–624. doi:10.1115/1.1486223.
URL http://dx.doi.org/10.1115/1.1486223

[76] Y. Matsumoto, T. Kanbara, K. Sugiyama, Y. Tamura, Numerical study of cavitating flow structure on a hydrofoil, in: 4th KSME-JSME Fluids Eng Conf., Pusan, Korea, 1998.

[77] W. Yuan, G. Schnerr, Cavitation in injection nozzles - effect of injection pressure fluctuations, in: CAV2001, 4th Int. Symposium on Cavitation, Pasadena, USA, 2001.

[78] Y. Tamura, K. Sugiyama, Y. Matsumoto, Cavitating flow simulations based on the bubble dynamics, in: CAV2001, USA, 2001.

[79] A. Kubota, H. Kato, H. Yamaguchi, A new modelling of cavitating flows: a numerical study of unsteady cavitation on a hydrofoil section, Journal of Fluid Mechanics 240 (1992) 59–96.

[80] E. Giannadakis, M. Gavaises, C. Arcoumanis, Modelling of cavitation in diesel injector nozzles, Journal of Fluid Mechanics 616 (2008) 153–193.

[81] A. Jamaluddin, G. Ball, C. Turangan, T. Leighton, The collapse of single bubbles and approximation of the far-field acoustic emissions for cavitation induced by shock wave lithotripsy, Journal of Fluid Mechanics 677 (2011) 305–341.

[82] K. Ando, T. Colonius, C. E. Brennen, Numerical simulation of shock propagation in a polydisperse bubbly liquid, International Journal of Multiphase Flow 37 (2011) 596–608.

[83] D. Fuster, C. T., Modelling bubble clusters in compressible liquids, Journal of Fluid Mechanics 688 (2011) 352–389.

[84] L. Yuan, Sonochemical effects on single-bubble sonoluminescence, Phys Rev E 72 (2005) 1–14.

[85] W. Moss, J. Levantin, A. Szeri, A new damping mechanism in strongly collapsing bubbles, Proc. R. Soc. Lond. A 456 (2000) 2983–2994.

[86] J. Buttenbender, P. Pelz, The influence of imposed strain rate and circulation on bubble and cloud dynamics, in: CAV2012, Singapore, 2012.

[87] Y. Lu, J. Katz, A. Prosperetti, Generation and transport of bubble clouds in high-intensity focused ultrasonic fields, in: CAV2012, Singapore, 2012.

[88] J. Dumond, F. Magagnato, A. Class, Stochastic-field cavitation model, Physics of Fluids 25(7). doi:https://doi.org/10.1063/1.4813813.

[89] M. B. Liu, J. R. Shao, Z. Shang, SPH modeling of supercavity induced by underwater high speed objects, in: 8th International Symposium on Cavitation, Singapore, 13th - 16th August, 2012.

[90] D. Varas, R. Zaera, J. López-Puente, Numerical modelling of the hydrodynamic ram phenomenon, International Journal of Impact Engineering 36(3) (2009) 363–374.
URL http://www.scopus.com/inward/record.url?eid=2-s2.0-57649187929&partnerID=40&md5=1fa1b75a20208151633b0b72e5af663f

[91] D. M. Bourg, Development of the distributed points method with application to cavitating flow, Ph.D. thesis, PhD Thesis, University of New Orleans (2008).

[92] G. Falcucci, S. Ubertini, G. Bella, S. Succi, Lattice boltzmann simulation of cavitating flows, Communications in Computational Physics 13 (2013) 685–695.

URL http://www.scopus.com/inward/record.url?eid=2-s2.0-84866306497&partnerID=40&md5=b7acba40be3fecf3aeeb938ee1dbac39

[93] V. Coralic, T. Colonius, Shock-induced collapse of a bubble inside a deformable vessel, European Journal of Mechanics B Fluids 40 (2013) 64–74.

[94] S. Adami, J. Kaiser, I. Bernejo-Moreno, N. A. Adams, Numerical modeling of shock waves in biomedicine (nanoshock): Proceedings of the 2016 summer program, Tech. rep. (2016).

[95] A. H. Koop, Numerical simulation of unsteady three-dimensional sheet cavitation, Ph.D. thesis, University of Twente, the Netherlands (2008).

[96] N. Kyriazis, P. Koukouvinis, M. Gavaises, Numerical investigation of bubble dynamics using tabulated data, International Journal of Multiphase Flow 93 (2017) 158 – 177. doi:https://doi.org/10.1016/j.ijmultiphaseflow.2017.04.004.
URL http://www.sciencedirect.com/science/article/pii/S0301932216307650

[97] R. A. Thompson, K.-P. Lee, R. N. Gupta, Computer codes for the evalutation of thermodynamic and transport properties for equilibrium air to 30000k, Tech. rep., Langley Research Center, Hampton Virginia (1991).

[98] B. J. McBride, G. Sanford, Computer program for calculating and fitting thermodynamic functions, Tech. rep., United States (1992).

[99] W. C. Moss, D. B. Clarke, J. W. White, D. A. Young, Hydrodynamic simulations of bubble collapse and picosecond sonoluminescence, Physics of Fluids 6.

[100] F. J. Heymann, High speed impact between a liquid drop and a solid surface, Journal of Applied Physics 40 (13) (1969) 5113–5122. arXiv:http://dx.doi.org/10.1063/1.1657361, doi:10.1063/1.1657361.
URL http://dx.doi.org/10.1063/1.1657361

[101] M. B. Lesser, Analytic solutions of liquid-drop impact problems, Proceedings of the Royal Society of London A: Mathematical, Physical and Engineering Sciences 377 (1770) (1981) 289–308. doi:10.1098/rspa.1981.0125.

[102] K. K. Haller, Y. Ventikos, D. Poulikakos, P. Monkewitz, Computational study of high-speed liquid droplet impact, Journal of Applied Physics 92 (5) (2002) 2821–2828. arXiv:http://dx.doi.org/10.1063/1.1495533, doi:10.1063/1.1495533.
URL http://dx.doi.org/10.1063/1.1495533

[103] A. V. Chizhov, K. Takayama, The impact of compressible liquid droplet on hot rigid surface, International Journal of Heat and Mass Transfer 47 (67) (2004) 1391–1401. doi:https://doi.org/10.1016/j.ijheatmasstransfer.2003.05.001.
URL http://www.sciencedirect.com/science/article/pii/S0017931003005659

[104] T. Sanada, K. Ando, T. Colonius, A computational study of high-speed droplet impact, Fluid Dynamics and Materials Processing 7 (4) (2011) 329–340. doi:10.3970/fdmp.2011.007.329.

[105] Y.-Y. Niu, H.-W. Wang, Simulations of the shock waves and cavitation bubbles during a three-dimensional high-speed droplet impingement based on a two-fluid model, Computers & Fluids 134135 (2016) 196–214. doi:http://doi.org/10.1016/j.compfluid.2016.05.018.
URL http://www.sciencedirect.com/science/article/pii/S0045793016301657

[106] G. Lacaze, A. Misdariis, A. Ruiz, J. C. Oefelein, Analysis of high-pressure diesel fuel injection processes using les with real-fluid thermodynamics and transport, Proceedings of the Combustion Institute 35 (2) (2015) 1603–1611.

URL http://www.sciencedirect.com/science/article/pii/S1540748914002302

[107] F. Örley, T. Trummler, S. Hickel, M. S. Mihatsch, S. J. Schmidt, N. A. Adams, Large-eddy simulation of cavitating nozzle flow and primary jet break-up, Physics of Fluids 27 (8) (2015) 86–101. arXiv:http://aip.scitation.org/doi/pdf/10.1063/1.4928701, doi:10.1063/1.4928701.
URL http://aip.scitation.org/doi/abs/10.1063/1.4928701

[108] A. Gnanaskandan, K. Mahesh, A numerical method to simulate turbulent cavitating flows, International Journal of Multiphase Flow 70 (2015) 22–34. doi:https://doi.org/10.1016/j.ijmultiphaseflow.2014.11.009.
URL http://www.sciencedirect.com/science/article/pii/S0301932214002298

[109] C. Greenshields, OpenFOAM - The Open Source CFD Toolbox - User Guide, OpenFOAM Foundation Ltd., 2nd Edition (21 May 2015).

[110] Zwart, P. J., Gerber, A. G., Belamri, T., A two-phase flow model for predicting cavitation dynamics., in: ICMF 2004 International Conference on Multiphase Flow, 2004.

[111] C.-T. Hsiao, G. L. Chahine, H.-L. Liu, Scaling effect on prediction of cavitation inception in a line vortex flow, Journal of Fluids Engineering 125 (1) (2003) 53–60. doi:10.1115/1.1521956.
URL http://dx.doi.org/10.1115/1.1521956

[112] J. Ma, C.-T. Hsiao, G. L. Chahine, Modelling cavitating flows using an Eulerian-Lagrangian approach and a nucleation model, Journal of Physics: Conference Series 656 (1) (2015) 012160.
URL http://stacks.iop.org/1742-6596/656/i=1/a=012160

[113] J. Ma, G. L. Chahine, C.-T. Hsiao, Spherical bubble dynamics in a bubbly medium using an eulerlagrange model, Chemical Engineering Science 128 (2015) 64 – 81. doi:https://doi.org/10.1016/j.ces.2015.01.056.
URL http://www.sciencedirect.com/science/article/pii/S0009250915000858

[114] E. Brennen C., Cavitation and Bubble Dynamics, 1995.

[115] G. H. Schnerr, I. H. Sezal, S. J. Schmidt, Numerical investigation of three-dimensional cloud cavitation with special emphasis on collapse induced shock dynamics, Physics of Fluids 20 (4) (2008) 040703. arXiv:https://doi.org/10.1063/1.2911039, doi:10.1063/1.2911039.
URL https://doi.org/10.1063/1.2911039

[116] P. Koukouvinis, H. Naseri, M. Gavaises, Performance of turbulence and cavitation models in prediction of incipient and developed cavitation, International Journal of Engine Research 18 (4) (2017) 333–350. arXiv:https://doi.org/10.1177/1468087416658604, doi:10.1177/1468087416658604.
URL https://doi.org/10.1177/1468087416658604

[117] J.-P. Franc, J.-M. Michel, Fundamentals of Cavitation, Kluwer Academic Publishers, 2005.

[118] D. R. van der Heul, C. Vuik, P. Wesseling, Efficient computation of flow with cavitation by compressible pressure correction, ECCOMAS, Barcelona, 2000.

[119] C. D. Munz, S. Roller, R. Klein, K. J. Geratz, The extension of incompressible flow solvers to the weakly compressible regime, Computers & Fluids 32 (2003) 173–196.

[120] H. Guillard, C. Viozat, On the behaviour of upwind schemes in the low mach number limit, Computers & Fluids 28 (1999) 63–86.

[121] A. Meister, Asymptotic single and multiple scale expansions in the low mach number limit, SIAM Journal on Applied Mathematics 60 (1999) 256–271.

[122] E. F. Toro, Riemann Solvers and Numerical Methods for Fluid Dynamics, A Practical Introduction, Springer Berlin Heidelberg, 2009.

[123] S. Schmidt, I. Sezal, G. Schnerr, M. Talhamer, Riemann techniques for the simulation of compressible liquid flows with phase-transistion at all mach numbers - shock and wave dynamics in cavitating 3-d micro and macro systems, no. 1238 in 46th AIAA Aerospace Sciences Meeting and Exhibit, American Institute of Aeronautics and Astronautics, 2008. doi:10.2514/6.2008-1238.
URL http://dx.doi.org/10.2514/6.2008-1238

[124] F. Moukalled, L. Mangani, M. Darwish, The Finite Volume Method in Computational Fluid Dynamics, An Advanced Introduction with OpenFOAM and Matlab, Vol. 113, Springer International Publishing, 2015. doi:10.1007/978-3-319-16874-6.

[125] R. Abgrall, R. Saurel, Discrete equations for physical and numerical compressible multiphase mixtures, Journal of Computational Physics 186 (2) (2003) 361–396. doi:https://doi.org/10.1016/S0021-9991(03)00011-1.
URL http://www.sciencedirect.com/science/article/pii/S0021999103000111

[126] R. Saurel, F. Petitpas, R. Abgrall, Modelling phase transition in metastable liquids: application to cavitating and flashing flows, Journal of Fluid Mechanics 607 (2008) 313–350.

[127] P. Koukouvinis, M. Gavaises, A. Georgoulas, M. Marengo, Compressible simulations of bubble dynamics with central-upwind schemes, International Journal of Computational Fluid Dynamics (2016) 1–12.

[128] W. Wagner, A. Pruß, The iapws formulation 1995 for the thermodynamic properties of ordinary water substance for general and scientific use, Journal of Physical and Chemical Reference Data 31 (2) (2002) 387–535. arXiv:http://dx.doi.org/10.1063/1.1461829, doi:10.1063/1.1461829.
URL http://dx.doi.org/10.1063/1.1461829

[129] E. Lemmon, M. McLinden, D. Friend, NIST Chemistry WebBook, NIST Standard Reference Database Number 69, 2005, Ch. Thermophysical properties of fluid systems.
URL http://webbook.nist.gov

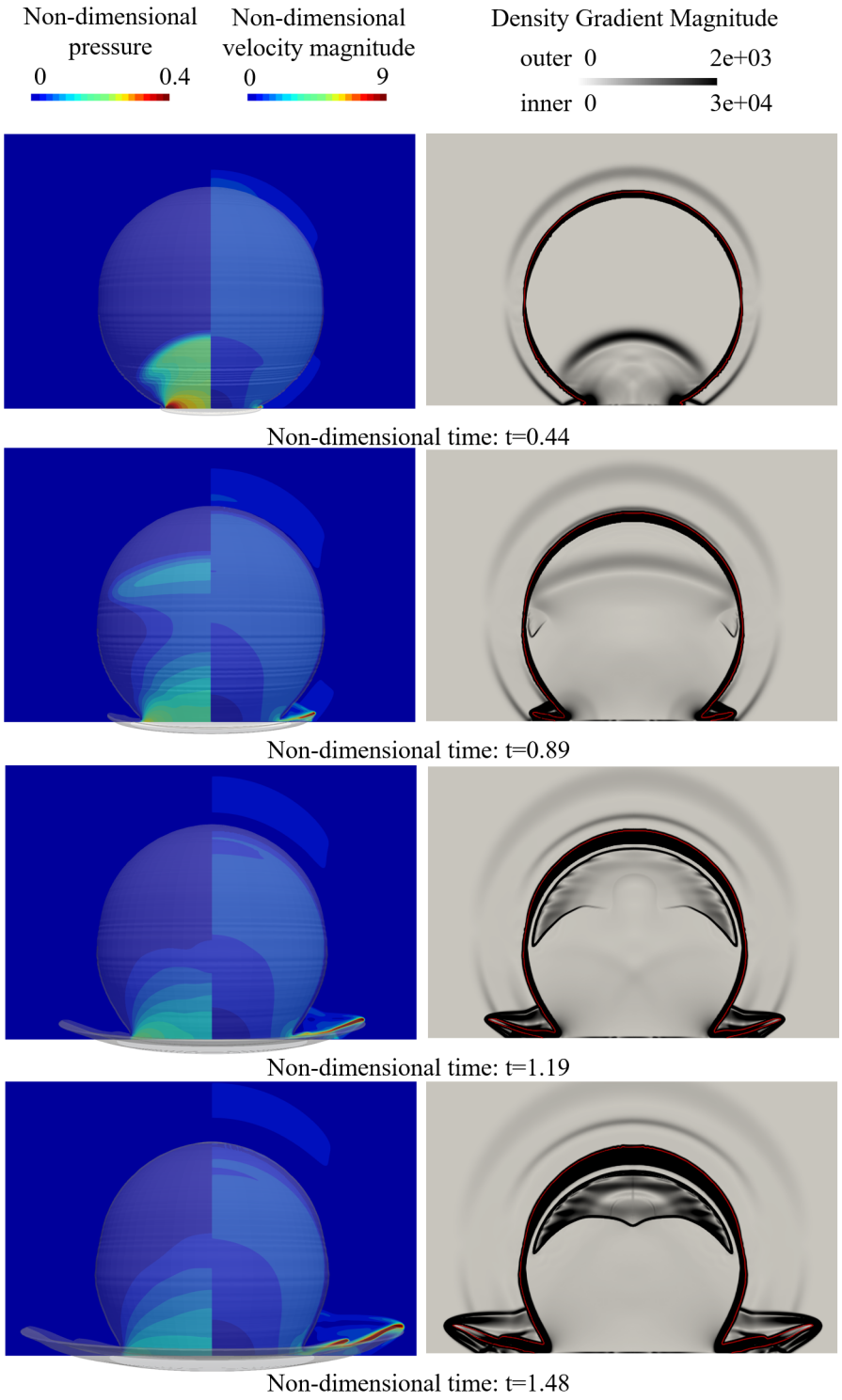

Figure 6: Drop impact at velocity $110\,m/s$. Left figure: Iso-surface of liquid mass fraction for $Y_g = 0.5$ combined with pressure (left half) and velocity magnitude (right half). Right figure: Density gradient magnitude, different scale for the interior and the exterior of the drop. Pressure and velocity are divided by p_{wh} and u_{imp} respectively, whereas time is measured from the moment of the impact and it has been non-dimensionalized with D/c_l.

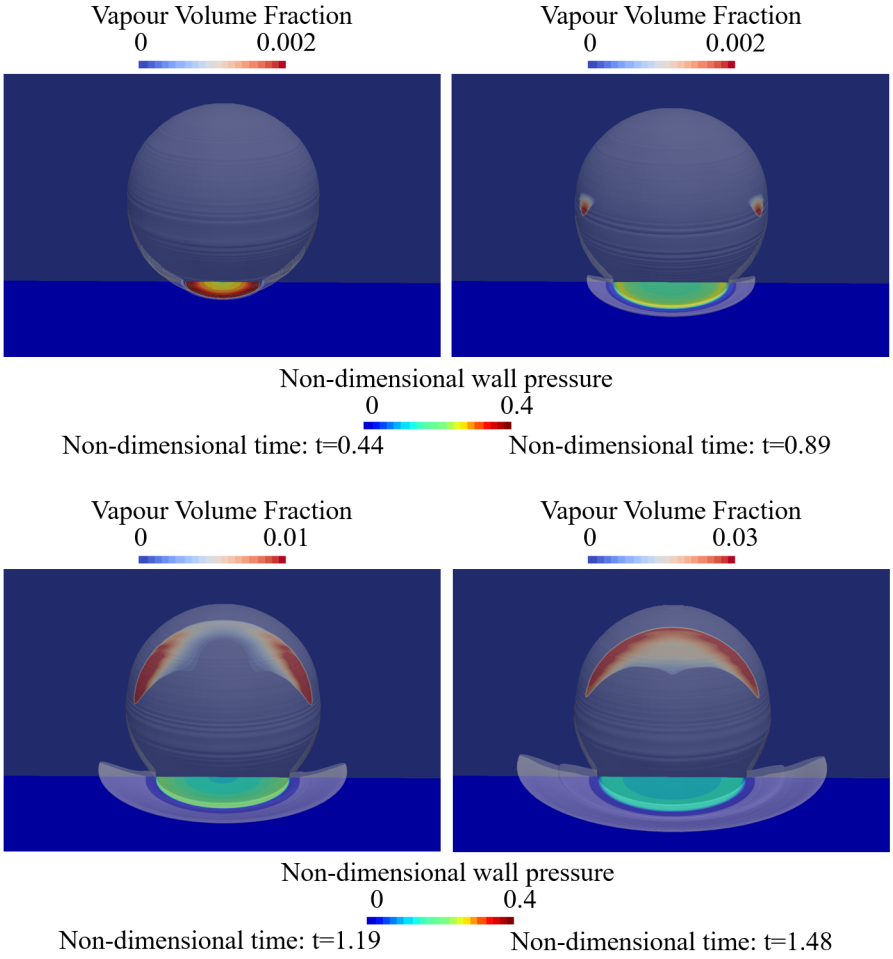

Figure 7: Drop impact at velocity $110\,m/s$. Iso-surface of liquid mass fraction for $Y_g = 0.5$ combined with wall pressure (lower part) and vapour volume fraction (upper part). Pressure is divided by p_{wh} and time is measured from the moment of the impact and it has been non-dimensionalized with D/c_l.

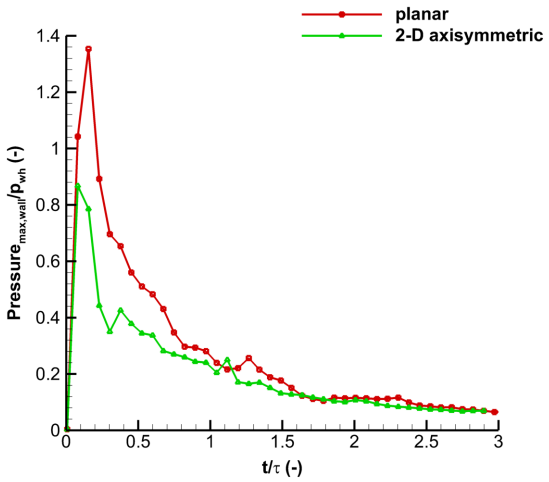

Figure 8: Comparison of the maximum wall pressure between a planar 2-D and a 2-D axisymmetric simulation at impact velocity $110\,m/s$. Wall pressure is non-dimensionalized with p_{wh} and time is measured from the moment of the impact and it has been non-dimensionalized with $\tau = D/c_l$.

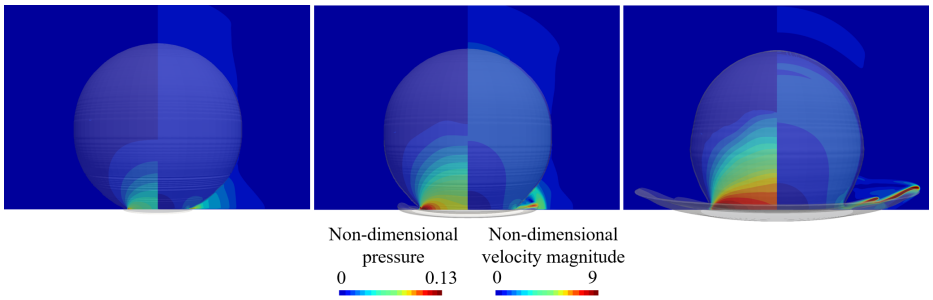

Figure 9: Comparison of the pressure (left slice) and the velocity magnitude (right slice) for $u_{imp} = 22.5\,m/s$ (left), $u_{imp} = 55\,m/s$ (middle) and $u_{imp} = 110\,m/s$ (right) at non dimensional time $t = 1.48$. The iso-surface of liquid mass fraction for $Y_g = 0.5$ is also shown. Pressure and velocity are divided by p_{wh} and u_{imp} respectively, whereas time is measured from the moment of the impact and it has been non-dimensionalized with D/c_l.

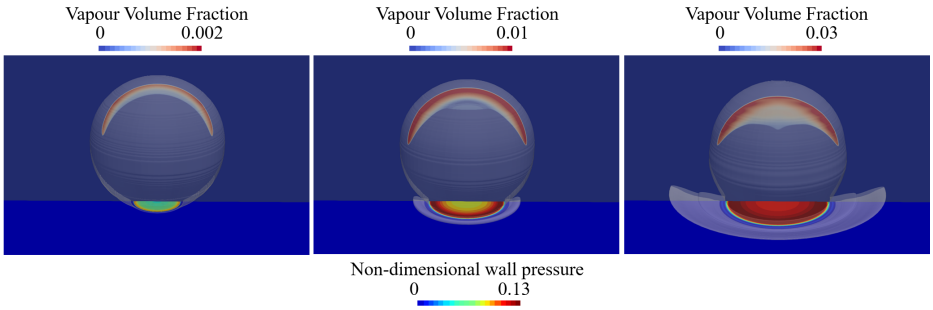

Figure 10: Comparison of the vapour volume fraction (upper) and wall pressure (bottom) for $u_{imp} = 22.5\,m/s$ (left), $u_{imp} = 55\,m/s$ (middle) and $u_{imp} = 110\,m/s$ (right) at non dimensional time $t = 1.48$. The iso-surface of liquid mass fraction for $Y_g = 0.5$ is also shown. Pressure is divided by p_{wh} and time is measured from the moment of the impact and it has been non-dimensionalized with D/c_l.

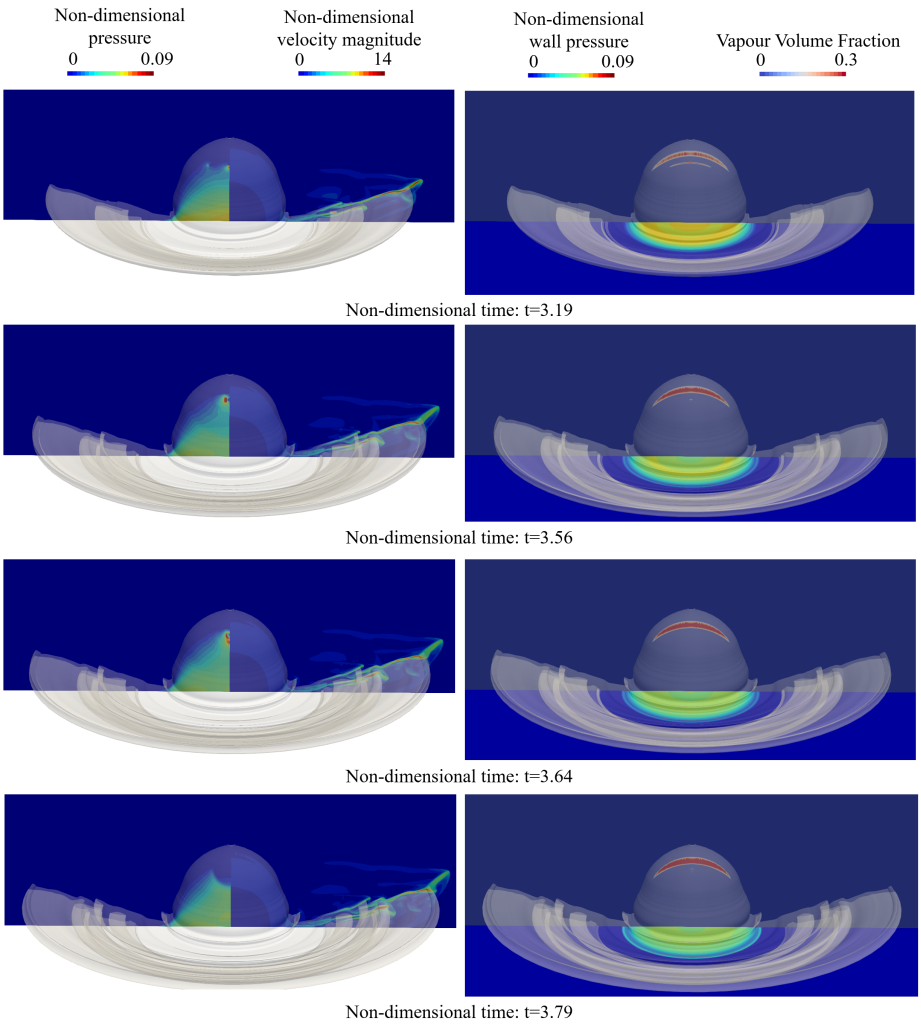

Figure 11: Later stage of drop impact at velocity $110\,m/s$. Left figure: Iso-surface of liquid mass fraction for $Y_g = 0.5$ combined with pressure (left slice) and velocity magnitude (right slice). Right figure: Iso-surface of liquid mass fraction for $Y_g = 0.5$ combined with wall pressure (bottom slice) and vapour volume fraction (upper slice). Pressure and velocity are divided by p_{wh} and u_{imp} respectively, whereas time is measured from the moment of the impact and it has been non-dimensionalized with D/c_l.

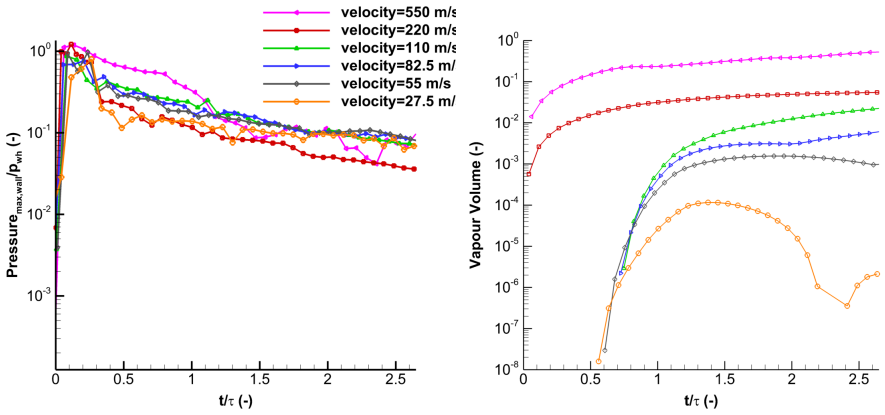

Figure 12: Maximum wall pressure (left) and generated vapour volume (right) with respect to time for different impact velocities. Wall pressure is divided by p_{wh}, time is measured from the moment of the impact and it has been non-dimensionalized with $\tau = D/c_l$, whereas vapour volume is divided by the initial drop volume.

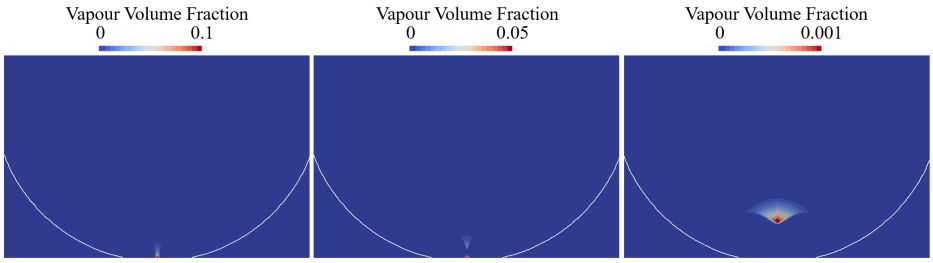

Figure 13: Close-up view of *case 8* at non-dimensional times $t = 0.15$ (left), $t = 0.18$ (medium) and $t = 0.25$ (right). Slices of vapour volume fraction combined with iso-line of liquid mass fraction for $Y_g = 0.5$ are shown. Time has been non-dimensionalized with D/c_l.

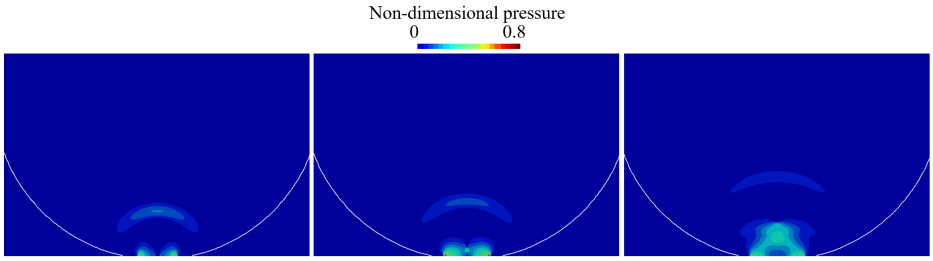

Figure 14: Close-up view of *case 8* at non-dimensional times $t = 0.15$ (left), $t = 0.18$ (medium) and $t = 0.25$ (right). Slices of pressure combined with iso-line of liquid mass fraction for $Y_g = 0.5$ are shown. Time has been non-dimensionalized with D/c_l and pressure with p_{wh}.

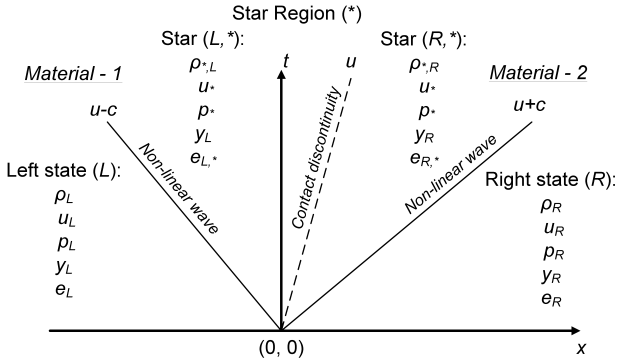

Figure A.15: Wave structure of the Riemann problem for the multi-material Euler equations for a general equation of state $p = f(\rho, e, Y)$.

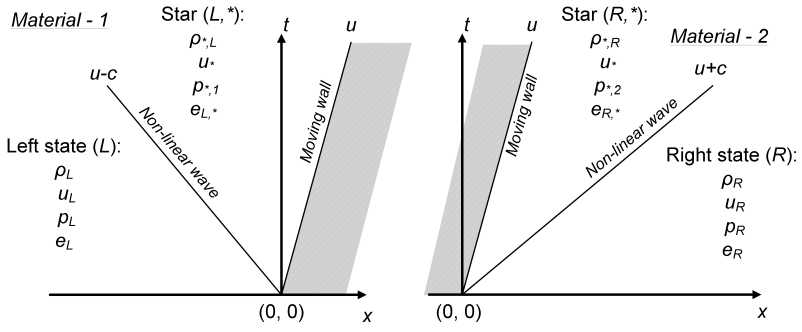

Figure A.16: Equivalent splitting of the multi-material Riemann problem to two coupled single-material Riemann problems.